# Silicon-based Materials as Negative Electrodes for Li-ion Batteries

by
Kaitlin Town

A thesis
presented to the University of Waterloo
in fulfillment of the
thesis requirement for the degree of
Master of Science
in
Chemistry

Waterloo, Ontario, Canada, 2014

**AUTHOR'S DECLARATION**

I hereby declare that I am the sole author of this thesis. This is a true copy of the thesis, including any required final revisions, as accepted by my examiners.

I understand that my thesis may be made electronically available to the public.

_____

Kaitlin Town

# ABSTRACT

Silicon is a promising negative electrode material for lithium-ion (Li-ion) batteries, with volumetric and gravimetric capacities much higher than those in current commercial batteries. Implementation of Si as a negative electrode is halted, however, by a large irreversible capacity and declining reversible capacity over cycle life. These problems are linked to the large volume expansion that Si undergoes when reacted with lithium, and overcoming them is the focus of this thesis.

To overcome this expansion, in the first part titanium silicides were proposed to buffer the volume expansion problem as Ti does not react with Li and is robust. A pure phase of the targeted TiSi and $TiSi_2$ was not achieved, however one product mixture containing $TiSi_2$ and $Ti_5Si_3$ was cycled against Li at C/20. A capacity of 715 mAh $g^{-1}$ was achieved, however rapid capacity fade occurred over the first 10 cycles.

The second part of the thesis focused on heterostructured Si-Ge and Ge-Si core-shell nanowires. The morphology of the nanowires allows for better accommodation of strain due to lithiation, and Ge functions as an active matrix, as it can store Li in a similar manner as Si. The specific capacities of the nanowires were good at 1346 mAh $g^{-1}$ and 1276 mAh $g^{-1}$, however after 50 cycles the Si-Ge nanowires had a capacity retention of 72.4 % and the Ge-Si retained 62.4 %. The diffusion coefficient of Li was determined from GITT and EIS to be within the range of $10^{-16}$ to $10^{-13}$ $cm^2s^{-1}$ and was slightly lower than other reported values, attributed to the dense structure of the nanowires slowing diffusion.

# ACKNOWLEDGEMENTS

I would like to extend my appreciation to my supervisor, Professor Linda F. Nazar, for her guidance throughout the course of this research project.

I would also like to extend my appreciation to other members of the research group past and present that have lent me their assistance and expertise: Dr. Marine Cuisinier, Dr. Rajesh Tripathi, Dr. Guerman Popov, Dr. Brian Ellis, Robert Black, Brian Adams, and Scott Evers.

Finally, I would like to thank my family and friends for all of their love and support.

# TABLE OF CONTENTS

# LIST OF FIGURES

# LIST OF TABLES

# GLOSSARY

| | |
|---|---|
| AC | Alternating current |
| CVD | Chemical vapour deposition |
| DEC | Diethylene carbonate |
| EC | Ethylene carbonate |
| EDX | Energy dispersive X-ray spectroscopy |
| EIS | Electrochemical impedance spectroscopy |
| GITT | Galvanostatic intermittent titration technique |
| OCV | Open circuit voltage |
| PITT | Potentiostatic intermittent titration technique |
| SEI | Solid electrolyte interphase |
| SEM | Scanning electron microscope |
| TEM | Transmission electron microscope |
| XRD | X-ray diffraction |
| 2032-type coin cell | 20 mm diameter, 3.2 mm height battery cell |

# Chapter 1

# Introduction

## 1.1 Motivation

The energy needs associated with global development and technological advancement thus far have been accommodated by combustible fuel sources. However, it is widely accepted that worldwide energy demands will continue to grow and traditional sources alone cannot meet these growing expectations due to environmental concerns with carbon dioxide emissions and global warming, and the increasing cost of oil due to heavy consumption of fossil fuels. The need for safe, reliable, environmentally responsible energy storage for both stationary and portable applications will continue to increase, placing greater importance on alternative energy sources such as photovoltaics and wind, which provide energy intermittently and therefore require reliable energy storage systems for load-leveling. Additionally, portable energy needs for both consumer electronics and electric vehicles must be met, with an emphasis on sufficient storage capacity in a minimum of space. Lithium-ion technology is the most promising candidate to accommodate these demands, with benefits in terms of weight, size, and design flexibility.

## 1.2 Rechargeable Li-ion Batteries

The lithium (Li)-ion cell is the most widely used form of secondary battery due to its high energy density, high operating voltage and low self-discharge when compared with nickel-cadmium or nickel-metal hydride cells. The advantage of using lithium metal within a battery was first demonstrated by M. S. Whittingham in the 1970s in a primary

cell composed of metallic lithium as a negative electrode and $TiS_2$ as a positive electrode, in which $Li^+$ ions were reversibly inserted.[1] As Li is the most electropositive and lightest metal, with an electrode potential of -3.04 V vs. the standard hydrogen electrode, molar mass ($M_W$) of 6.94 g $mol^{-1}$, and density ($\rho$) of 0.534 g $cm^{-3}$, it can allow for an energy storage system with a high energy density and high operating voltage. However, repeated cycling of a secondary cell containing a pure Li metal negative electrode results in dendritic growth of Li from the electrode through separator materials within the cell, which can cause short-circuiting and pose a safety hazard. The increased surface area of the electrode also causes increased side reactions with electrolyte, resulting in a decreased cycle life.

A secondary battery consists of a positive electrode and a negative electrode at separate poles of the cell. These electrodes are occasionally referred to as cathodes and anodes, however both electrodes undergo reduction and oxidation reactions depending on the state of charge of the battery, thus a simpler convention is to refer to the electrode with the lower potential as the negative electrode, and the higher potential as the positive electrode. The two electrodes are physically separated, however an ionically-conductive, electronically-insulating electrolyte medium allows $Li^+$ movement in the cell.

A "rocking chair" battery employs lithium insertion materials at both the positive and negative electrode (**Figure 1.1**), and is based upon the reversible insertion or intercalation, and removal or de-intercalation of $Li^+$ ions from the host materials. The use of insertion materials limits the possibility of dendritic Li growth. When the two electrodes are connected externally to the cell, the electronic circuit is complete and electrons can be chemically produced at the negative electrode, flow through the external

connection, and recombine with $Li^+$ ions that migrate through the cell to the positive electrode. Lithium atoms at the surface of the electrode diffuse into the electrode due to an existing concentration gradient. Therefore, Fick's law of diffusion can be applied.

During cell discharge this process occur spontaneously, allowing chemical energy to be harnessed. Application of an external current will reverse discharge reactions and the movement of ions and electrons within the cell, hence the terminology of "rocking chair" battery.

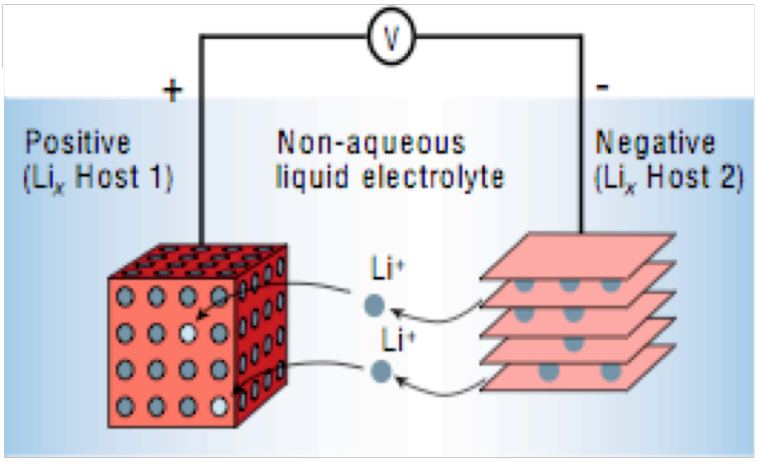


**Figure 1.1 Schematic diagram of a Li-ion cell.[2]**

The amount of electrical energy that a cell can provide is directly related to the chemical reactions at each electrode, as the cell voltage is the difference in operating potentials of the positive and negative electrodes. Therefore, an effective method for improving the capacity and energy density of a cell is to improve upon and replace the materials used as electrodes, to allow for more lithium storage and extraction safely and reversibly.

### 1.2 Development of Negative Electrode Materials

As discussed above, early Li-based batteries employed metallic lithium as a negative electrode, which was abandoned for safety concerns. The next major development in the field occurred in 1981, when the graphite anode was patented by Bell Labs. Graphite has a theoretical capacity of 372 miliampere hours per gram (mAh $g^{-1}$), and incorporates lithium between sheets in its structure, preventing the formation of dendrites. Additionally, cells that employ graphite can be assembled in a discharged state, which provides safety for storage and transport.

In 1991, Sony commercialized a Li-ion battery that used carbon-based materials with a theoretical capacity of 372 mAh $g^{-1}$ as a negative electrode and a positive electrode containing $LiCoO_2$ and derivatives, which has a theoretical capacity of 135 mAh $g^{-1}$. As previously stated, the graphitic negative electrode was discovered a full decade earlier, indicating a lack of development of suitable negative electrode materials in the interim decade. To harness the full potential of the Li-ion battery, high capacity negative electrode materials must be developed to match advanced cathode systems to be a viable power storage source for future high-energy devices.

### 1.3 Silicon as a Negative Electrode Material

Since Dey demonstrated that Li metal could electrochemically alloy with other metals[3], Li-alloys have been heavily investigated as potential negative electrode materials. Among the many Li alloy elements possible, Group 14 elements such as Sn and Si have been a promising focus due to their Li storage ability and associated high capacity. In 2005 Sony launched the Nexelion battery, which uses a tin-based negative electrode. The production of the Nexelion cell has since been viewed as a benchmark,

which suggested that similar materials, termed "alloy" materials, would replace carbonaceous materials as negative electrodes.[4]

As silicon possesses a high natural abundance, high theoretical capacity, and low discharge potential when compared with Li, it has been the most widely researched element within the group. Several Li-Si line-phase compounds exist (**Figure 1.2**), with theoretical capacities much higher than those of carbon-based materials (**Table 1.1**).

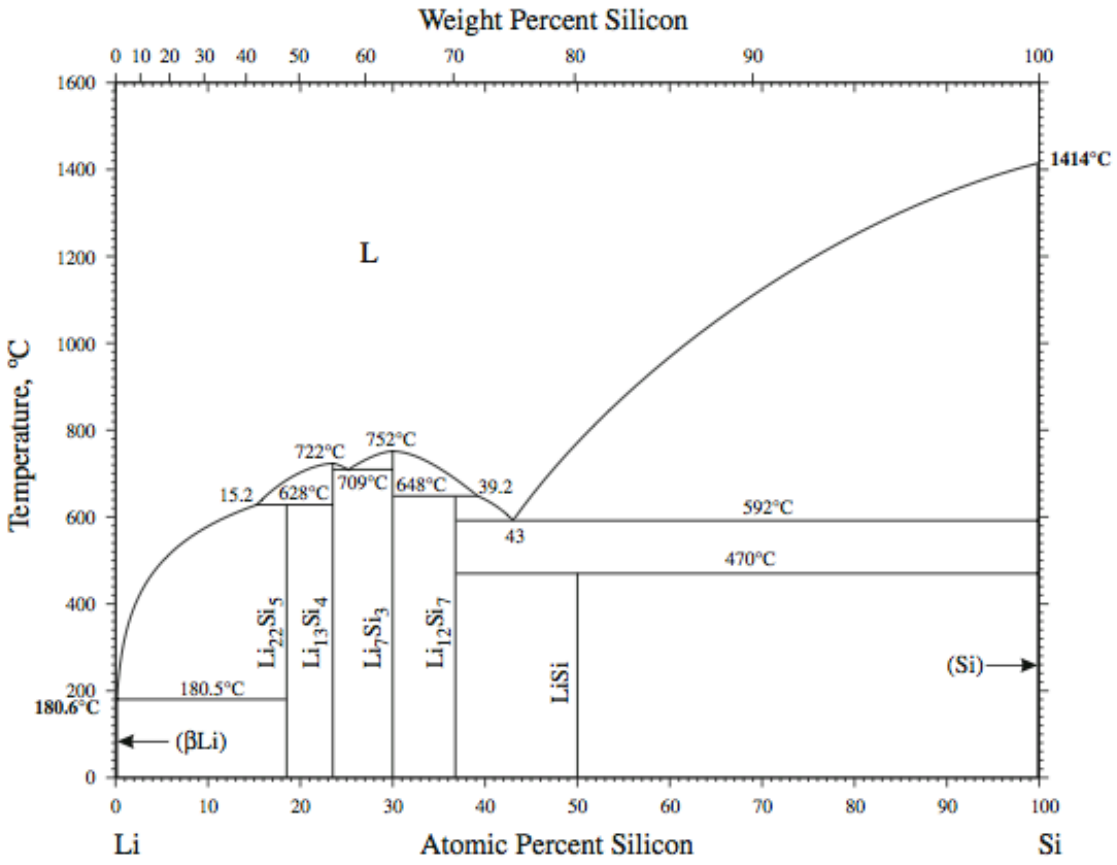


**Figure 1.2 Phase Diagram of the Li-Si system.[5]**

| Intermetallic | Molar volume ($cm^3/mol$) | Gravimetric Capacity (mAh/g) | Volumetric Capacity ($mAh/cm^3$) | Equilibrium discharge potential (V) | Equilibrium charge potential (V) |
|---|---|---|---|---|---|
| $Li_{12}Si_7$ | 26.21 | 1641 | 1757 | 0.332 | 0.52 |
| $Li_7Si_3$ | 31.00 | 2234 | 2023 | 0.288 | 0.52 |
| $Li_{13}Si_4$ | 40.53 | 3111 | 2155 | 0.158 | 0.43 |
| $Li_{22}Si_5$ | 49.62 | 4212 | 2383 | 0.044 | 0.30 |

**Table 1.1 Line phase compounds of the Li-Si system.[6]**

### 1.3.1 Electrochemical Lithiation of Silicon

At room temperature, several of the line-phase Li-Si compounds are not electrochemically available from the lithiation of silicon. Instead, silicon undergoes a phase transition from crystalline to amorphous (reaction 1). The resultant lithiated amorphous silicide then recrystallizes at very low voltages[7] as the metastable material, $Li_{15}Si_4$ (reaction 2). $Li_{15}Si_4$ has a theoretical capacity of 3.75 Li per Si, and gravimetric (3572 mAh $g^{-1}$) and volumetric (8330 $mAh/cm^3$)[8] capacities greater than other lithium uptake reactions.

$$Si\ (crystalline) + xLi^+ + xe^- \rightarrow Li_xSi\ (amorphous) \quad (1)$$

$$4\ Li_xSi\ (amorphous) + 4\ (3.75\text{-}x)Li^+ + 4\ (3.75\text{-}x)e^- \rightarrow Li_{15}Si_4\ (crystalline) \quad (2)$$

As Si is lithiated, a rapid decrease in voltage can be observed in the charge-discharge profile until just below 0.2 V (vs. $Li/Li^+$, **Figure 1.3)**, followed by a long plateau region. The transition from crystalline Si to amorphous $Li_xSi$ is a two-phase process, where the observed plateau is associated with the formation of Li-silicides. Crystallization of the $Li_{15}Si_4$ phase occurs around 50 mV. In the first charge-discharge cycle of a bulk Si anode, a charge capacity of 3260 mAh $g^{-1}$ and a discharge capacity of 1170 mAh $g^{-1}$ are obtained, resulting in a Coulombic efficiency of 35%.[9] Subsequent

cycles show more sloped plateau regions, indicating a single-phase region that corresponds to a reaction between amorphous $Li_xSi$ and $Li_{15}Si_4$.

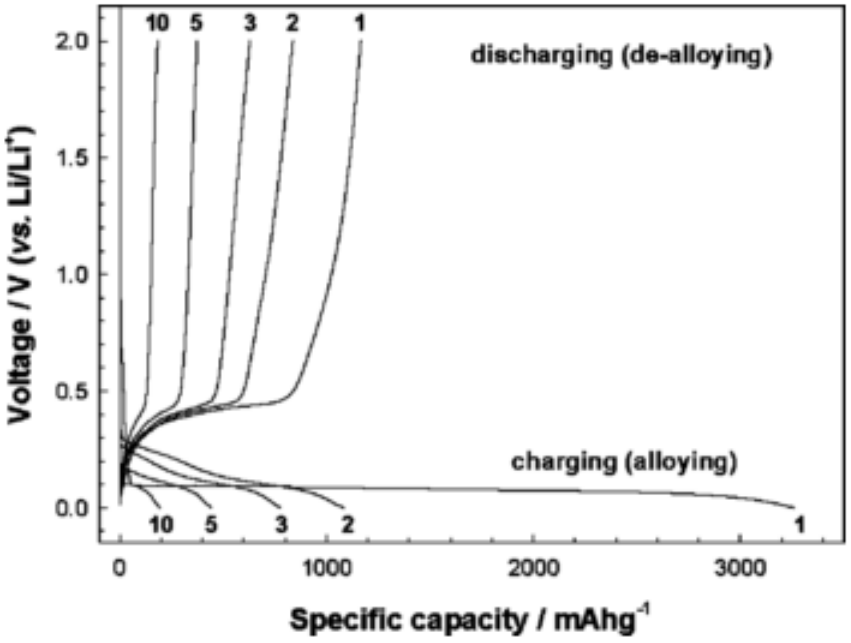


**Figure 1.3 Galvanostatic charge/discharge profile of micro-Si.[10]**

### 1.3.2 Challenges with Silicon Electrodes

Despite the low cost and high specific capacity of Si, commercial rechargeable batteries with Si-based electrodes have not been produced due to a capacity fade after several tens of cycles, related to large volume changes of approximately 300% that occur during lithiation and de-lithiation.

The volume changes observed in a Si electrode from the lithiation/de-lithiation process causes an increase in internal resistance of the electrode, and thus lead to successive capacity loss after few cycles. During the lithiation of bulk Si, expansion occurs and the electrical resistance of the active material decreases due to the formation of Li-Si systems, which are more electronically conductive than pure silicon. In the de-lithiation step the contact resistance and the charge transfer resistance increase, due to the

volume contraction of the material that is accompanied by a loss of electronic contact between the active material particles. Due to this loss of contact, complete de-lithiation is not possible because of electrical isolation of some small particles containing Li.

Additionally the volume changes that occur within the material cause stress on the particles, causing cracking and a modification of the electrode. These cracks increase the surface area of the electrode that is exposed to the electrolyte, leading to an increase in the amount of solid electrolyte interphase (SEI) that is formed. This increase in SEI raises the internal resistance of the cell, and causes the irreversible capacity to increase. The irreversible capacity is associated with the use of $Li^+$ and electrons to form the SEI layer, which reduces the amount of lithium available for cycling within the cell.

The SEI is a region that forms in the battery cell on the surface of a positive or negative electrode in contact with the cell's electrolyte, and is composed of reductive decomposition products of the electrolyte. This decomposition occurs as the silicon negative electrode operates at low potentials relative to metallic lithium, and the electrolyte is outside its thermodynamic stability region. The solvent and salt of the electrolyte are reduced, and these insoluble reduction products form a film on the electrode. The SEI of graphite-based electrodes has been studied, and is known to aid in stability due to surface passivation.

### 1.4 Methods to Overcome Volume Expansion

Several approaches have been employed to overcome the impact of volume expansion upon lithiation of Si, with varying degrees of effectiveness. A supporting matrix that does (active) or does not (inactive) engage in lithiation can act as a buffer to lend structural support, as well as maintaining electronic contact in a manner similar to

conductive additives. However, to prove effective active matrices must not demonstrate the same volume changes as Si, and inactive matrices must be rigid enough to withstand stress from the expanding Li-Si.[11,12]

Decreasing structures to the nano-scale has been shown effective, as it decreases the stress placed on particles due to the volume change, resulting in fewer cracks of the electrode and limited SEI formed.[13]

Inclusion of a void within the electrode structure to accommodate volume changes due to lithiation/delithiation is a similar technique. It was well-employed by Magasinski *et al*.[14] in a highly porous Si/C structure, which displayed a specific capacity of Si nanoparticles of approximately 3670 mAh $g^{-1}$, the highest reported, with a coulombic efficiency of 100%. At discharge rates of 1C and 8C the capacity was 1590 and 870 mAh $g^{-1}$ respectively. These relatively high rate capabilities indicate good reaction kinetics, further supported by a narrow, intense peak at 0.5 V in the differential capacity curve, associated with Li extraction.

### 1.5 Scope of this Thesis

In this thesis, different Si-containing materials are evaluated as potential negative electrode materials for Li-ion batteries. The literature review in Chapter 1 gives an overview of Li-ion batteries and the characteristics of select negative electrode materials. Chapter 2 contains a description of the experimental procedures and characterization methods used in my project.

Chapter 3 presents the attempted synthesis and electrochemical performance of targeted titanium silicides. The desired compounds were not synthesized in a pure phase, however the electrochemical performance of a promising product mixture was evaluated.

Chapter 4 details the morphology and electrochemistry of Si-Ge heterostructures obtained by a vapor-liquid-solid growth on a stainless steel substrate. Microscopy techniques were used to determine the morphology of the materials, and the materials were electrochemically evaluated through galvanostatic cycling, potentiostatic intermittent titration technique, galvanostatic intermittent titration technique and electrochemical impedance spectroscopy.

# Chapter 2

## Characterization Techniques

### 2.1 Overview

In introductory materials science classes, it is often stated that a material's structure determines its function. Therefore structural characterization is required to follow synthesis, using diffraction, microscopy, and spectroscopic techniques. These methods can provide structural information ranging from particle size and morphology to atomic composition and ordering. Subsequent sections within this chapter will outline the basic principles of characterization methods used in this study.

### 2.2 Powder X-ray Diffraction

X-ray diffraction (XRD) is a widely used tool for the characterization of atomic structure within a crystalline compound. This characterization is achieved through the application of Bragg's Law[15] (**Equation 2.1**), which relates the appearance of a diffraction pattern from incident X-rays with the crystal planes in a compound.

$$n \cdot \lambda = 2 \cdot d \cdot \sin\theta \qquad (2.1)$$

When atoms or molecules within a compound occur in regular repeating intervals, they can be viewed as a series of semi-transparent mirrors. When X-ray radiation is applied to the compound, beams of radiation can be reflected from adjacent planes. **Figure 2.1** shows parallel incident X-ray beams with a wavelength λ being diffracted by the atoms in the compound. Due to the increased distance that some beams must travel, an increased path length of 2dsinθ must exist for constructive overlap of the diffracted beams to occur, with the distance between the planes defined as d. If the angle between

the incident beam and crystal planes is not θ, the difference in path length changes and destructive interference occurs between the diffracted beams.

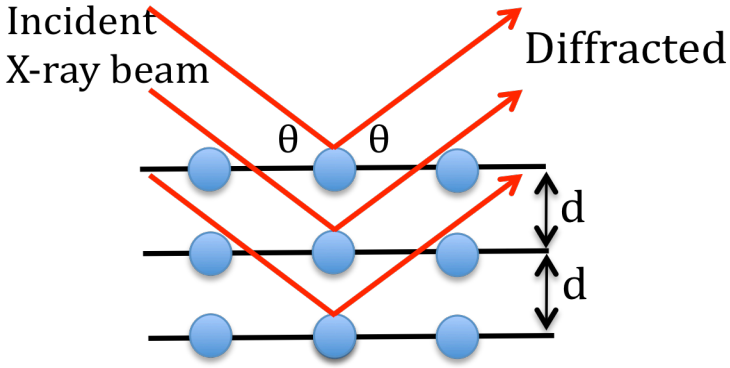


**Figure 2.1 Illustration of Bragg's Law.**

When powder XRD is conducted, the sample consists of many randomly oriented small crystals, of which some will be correctly aligned for Bragg diffraction to occur. During collection, the sample platform is rotated with respect to the incident X-ray beam and a pattern of the characteristic diffractions is obtained.

Powder XRD patterns were collected using a Bruker D8-Advance powder diffractometer equipped with a Vantec-1 detector, using Cu-K$\alpha_1$ radiation ($\lambda$ = 1.5406 Å). To minimize potential oxide layer formation, the powder samples were loaded under argon into a hermetically sealed holder equipped with a zero background silicon plate.

### 2.2 Scanning Electron Microscopy

Scanning electron microscopy (SEM) is an important characterization method for the determination structural information such as morphology, topology and particle size of a sample. In SEM, a high energy electron beam is rastered over the surface of a conductive sample to produce an image. Once the incident electron beam contacts the sample, electrons may be scattered elastically from the sample with no loss of energy, or

inelastically scattered with a slight reduction of energy, known as backscattered electrons (**Figure 2.2**). The electrons may also be absorbed by the sample, resulting in the production of low energy secondary electrons and X-rays. Elements with a higher atomic number scatter electrons more strongly, resulting in a brighter backscattered electron image.

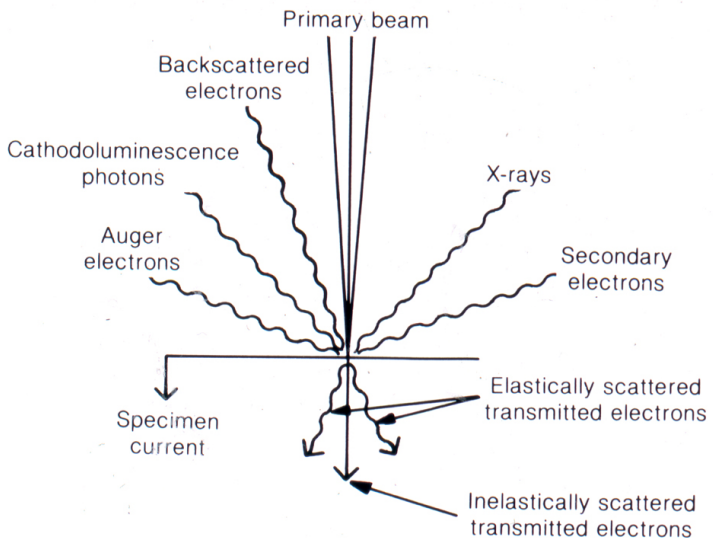


**Figure 2.2 Signals resulting from interaction of incident (primary) beam with specimen.**[16]

Elemental analysis of a sample can be conducted using SEM and examining the X-rays emitted. As these X-rays are generated through electron shell rearrangement, their energy is characteristic to the elements present. By scanning the energy of the emitted X-rays, elements with an atomic number above 4 can be detected. This method is known as elemental dispersive X-ray analysis (EDX).

SEM images were collected with a LEO 1530 field-emission SEM instrument and a Zeiss UltraPlus field-emission SEM instrument. Less conductive powder samples were gold coated (about 10 nm) to increase conductivity and limit surface charging from the

electron beam. Images in this thesis were collected by backscattered electron mode for titanium silicide compounds, and in-lens mode for nanowires.

### 2.3 Transmission Electron Microscopy

Transmission electron microscopy (TEM) also uses a focused electron beam to image a sample. However in TEM, a small cross section of a sample is examined and the electrons pass through the sample (**Figure 2.2**); atoms in the sample diffract electrons as the beam is passed through. The TEM image is generated from electrons that transmit through the sample and strike the detector. Sections of the sample that transmit more electrons appear bright in the image, while dark areas result from fewer transmitted electrons. TEM images were collected with a field-emission transmission electron microscope (FE-TEM, JEM 2100F, JEOL).

### 2.4 Raman Spectroscopy

Raman spectroscopy is a form of vibration spectroscopy, in which a change in the dipole moment of a compound is observed via the Raman effect. Three types of scattering are possible with Raman scattering (**Figure 2.3**). Elastic scattering, in which most of the light is scattered with the same frequency as the incident beam is known as Rayleigh scattering, and is not used. In-elastic scattering can occur with either a lower or higher frequency than the original source, known as Stokes and anti-Stokes scattering respectively. This decrease or increase in frequency results from the energy difference between the ground electronic state and the vibrational states of a molecular bond, and is characteristic of the bond. Anti-Stokes scattering is observed when a molecular bond is vibrationally excited prior to irradiation, and less frequently observed than Stokes

scattering. Raman spectroscopy was performed with a LabRam HR system (HORIBA Jobin Yvon), using 633 nm laser irradiation.

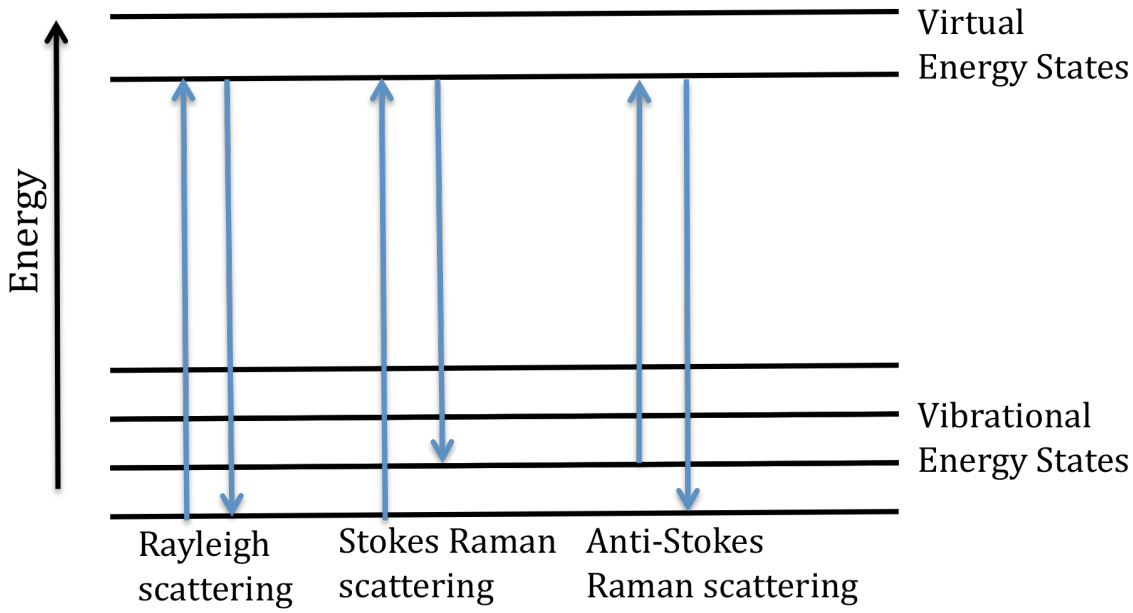


**Figure 2.3 The three types of Raman scattering.**

### 2.6 Electrochemistry

If an electrochemical system is subjected to the passage of a current between two electrodes, then it is not at equilibrium. The insertion and removal of ions and charge compensating electrons into and from a host material is a reversible process, used to study the transport mechanism of the ions and ultimately the suitability of the host material as an electrode. In the case of half cells - an active electrode material assembled in a battery against lithium metal - the processes of a single working electrode are examined. This examination can be achieved by controlling the current that passes through the cell, known as galvanostatic control, or by controlling the cell potential, known as potentiostatic control. The other electrode within the cell is used as a counter electrode to complete the electrical circuit. All electrochemical experiments were conducted on a VMP3 potentiostat system (Bio-logic) at room temperature.

### 2.6.1 Galvanostatic Cycling

The electrochemical characteristics of a battery such as specific capacity, cycling stability, and rate capability can be determined from the galvanostatic charge and discharge of a cell. In this method, a constant current is applied between the working and counter electrodes until a set potential limit is achieved. The rate at which a cell is galvanostatically cycled is referenced to as a fraction of C; A rate of 1 C is the current necessary to incorporate the theoretical maximum charge in 1 h.

The theoretical specific capacity, Q, of a material at a given current flow is related to the molar mass, Mw, of the compound:

$$Q = \frac{nF}{3.6Mw}$$

where F is Faraday's constant (96 485 C $mol^{-1}$) and the specific capacity is given in units of mAh $g^{-1}$. As a cycling rate of nC should yield the charge or discharge of the total theoretical capacity within 1/n hours, the real capacity can be calculated by:

$$Q = \frac{It}{m}$$

where I is the applied current, t the time and m the mass of active material.

As a constant current is applied to a cell, the composition of the electrode material changes

$$\Delta x = \frac{Mw}{zmF}\int_0^t Idt$$

with Δx representing the change in lithium concentration within the host material, and z the number of electrons transferred per ion, which is 1 for $Li^+$. For intercalation materials, a common practice is to plot the cell voltage against x to yield the voltage profile of the host material. The shape of the voltage profile can yield information about

the mechanism of lithiation. A single phase compound, or solid solution, will exhibit no strong attractive or repulsive interaction between lithium ions or the lithiation site and display a sloping curve. Comparatively, a two-phase reaction will have strong interactions which causes the formation of a phase boundary. The voltage profile will show a plateau of potential for the bi-phasic region of the system. In the case of silicon and other alloy-type materials a solid solution exists over the majority of the voltage profile, however the formation of line phase compounds occurs during a two-phase region.

### 2.6.2 Potentiostatic Intermittent Titration Technique

In potentiostatic intermittent titration technique (PITT), a voltage is applied to the electrochemical cell, while the current flow is measured in response. The voltage is changed by small, fixed increments usually around 0.01 V, after which the system is allowed to relax for a set period of time, or until the current reaches a small, non-zero, steady-state value (**Figure 2.4**). In this technique the system is assumed to be at equilibrium, from which it is perturbed by stepping the potential.

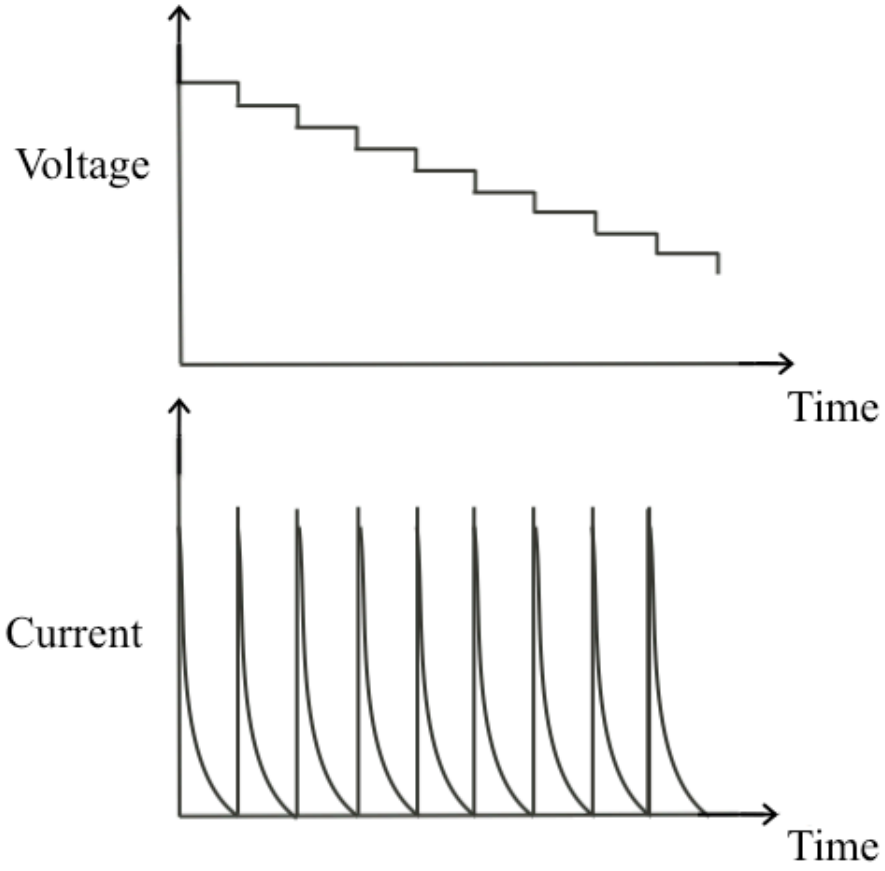


**Figure 2.4 Schematic of potential steps (top) and corresponding current response (bottom) during PITT.**

As with galvanostatic cycling, the nature of lithiation/delithiation of the material can be distinguished between solid solution and two-phase behaviour. In a solid solution, the current will decay exponentially from a step in voltage due to diffusion of the lithium ions. For a two-phase material, a constant current will be observed due to the difference between the voltage applied and the potential at the phase boundary. As the lithium ions are unable to diffuse through the phase boundary, a constant current results.

### 2.6.3 Galvanostatic Intermittent Titration Technique

Galvanostatic intermittent titration technique (GITT) was developed by Weppner et al.[17] to characterize the kinetics of the electrochemical formation of lithium-metal alloys. In GITT, a small current pulse is applied to the electrochemical system, followed by a period of open circuit voltage (OCV). The potential of the system is allowed to fluctuate in response to the pulsed current. Lithium ions are incorporated into (or removed from) the host material as a result of the applied current, and the potential of the system decreases (or increases) from the initial steady-state value. During the periods of OCV, the system reaches a new steady-state potential (**Figure 2.5**).

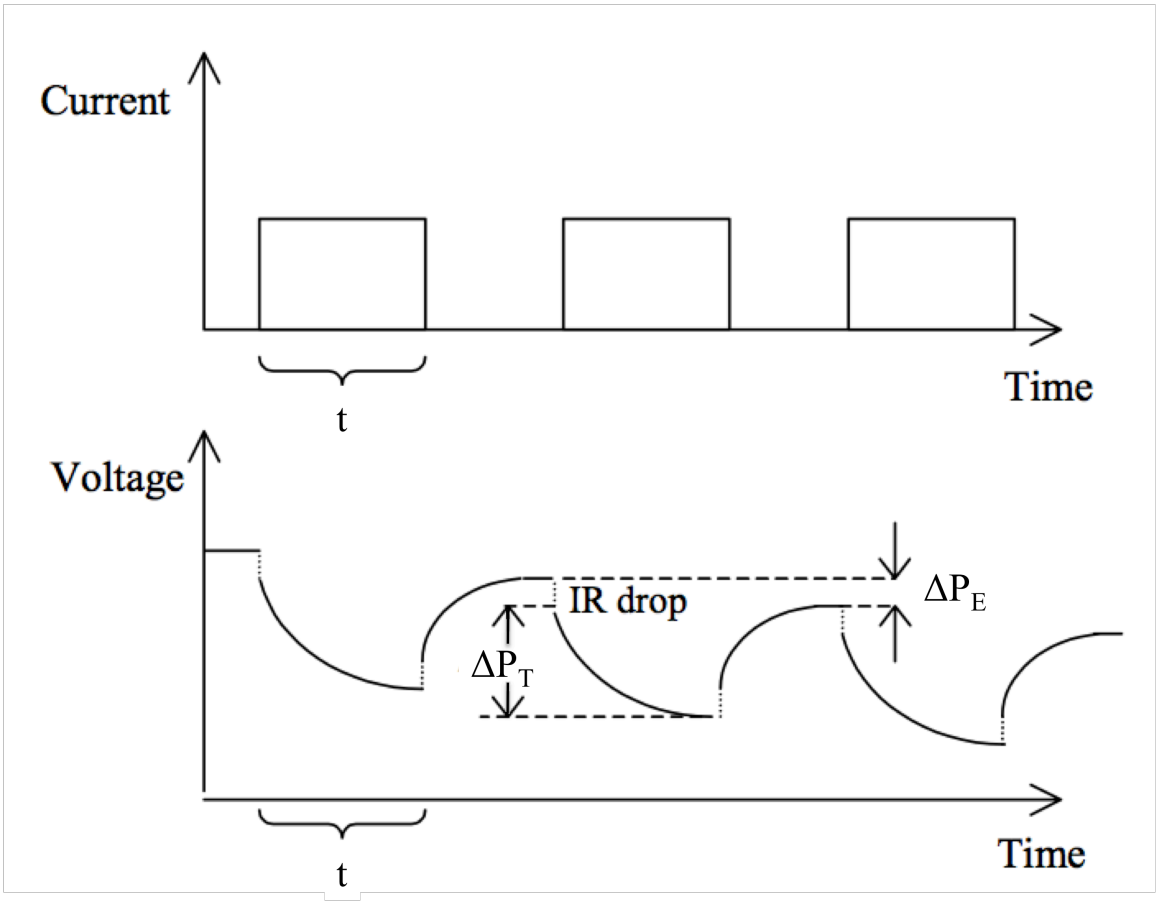


**Figure 2.5 Schematic of current (top) and corresponding voltage (bottom) profiles during GITT.**

As a current pulse is applied for time t, the total change in potential $\Delta P_T$ is observed. The IR drop represents the decrease in voltage due to resistance of the electrolyte and SEI. The difference in equilibrium potentials between pulses is noted as $\Delta P_E$.

By measuring the system's response to and relaxation from the applied current, the diffusion coefficient of lithium ions into the electrode material, $D_{Li^+}$, can be calculated. As this calculation is dependant upon the relationship between potential and composition, reliable $D_{Li^+}$ values cannot be obtained for two-phase regions as the potential is independent of composition in those systems.

### 2.6.4 Electrochemical Impedance Spectroscopy

Ohm's Law defines resistance, R, as the ratio between voltage, E, and current, I, for an ideal resistor:

$$R = \frac{E}{I}$$

A real world circuit contains elements that exhibit more complex behaviour, for which the property of impedance is adopted. Impedance is the measurement of a circuit's ability to resist the flow of electrical current, and is mathematical defined by the ratio of voltage across a cell and the corresponding current flowing through the system:

$$Z = \frac{E(\omega)}{I(\omega)}$$

with an angular frequency $\omega=2\pi f$, and f corresponding to the frequency.

Electrochemical impedance (EIS) is measured by applying an alternating current (AC) potential to an electrochemical cell, and measuring the current response. This AC

potential is applied as a sinusoidal excitation over a large frequency domain, and the current response is measured. In a linear or pseudo-linear system, the current response to a sinusoidal potential will be a sinusoid at the same frequency, but shifted in phase.

EIS data is commonly analyzed by fitting an equivalent electrical circuit model consisting of common electrical elements such as resistors, capacitors, and inductors. These elements in the model have a basis in the physical electrochemistry of the system.

### 2.6.5 Cell Assembly

All electrochemical tests were conducted using Swagelok$^{TM}$-type cells, as seen in **Figure 2.6**. The electrode material was placed in the bottom of the cell assembly, followed by two electronically insulating glass fibre separators (Whatman) which were saturated with electrolyte solution. Lithium metal was used as a negative electrode for all tests, and was followed by a stainless steel disc. A spring was used in the cell body to ensure good contact between all components, and a polyamide sheet (Kapton) was used inside the cell to electrically insulate the cell components from the stainless steel housing. As lithium is air and water sensitive, all cells were assembled in an argon-filled glovebox to prevent oxidation.

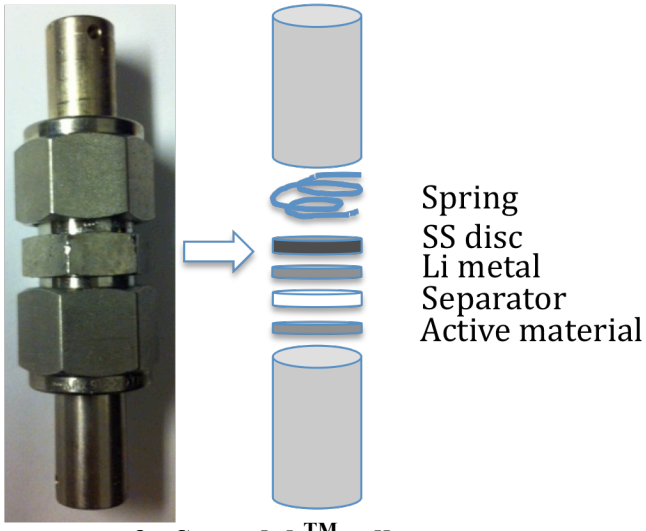


**Figure 2.6 Components of a Swagelok™ cell.**

# Chapter 3

## Titanium silicides

### 3.1 Motivation

#### 3.1.1 Literature Review

Increasing the coulombic efficiency, thus decreasing the capacity fade, of silicon-based negative electrodes is crucial in the development of higher-capacity batteries for commercial applications. Nano-scaled metal silicides possess high electrical conductivities, and can be employed as an inactive matrix material to compliment the properties of Si mentioned in Chapter 1. The inclusion of lithium-inactive metal within the electrode structure would improve electronic contact, reducing the need for other conductive additives, and additionally buffer the volume changes of the active Si phase.

Various inactive binary metal silicides such as $CaSi_2$, $CoSi_2$, $FeSi_2$, FeSi, $NiSi_2$ and NiSi have been probed as potential electrode materials.[18] As a proof of concept, metallic Li was found to alloy with Si in the disilicide compounds, with $CaSi_2$ displaying the greatest specific capacity of 320 mAh $g^{-1}$; however a capacity fade of 80% was observed after 10 cycles. This was attributed to both electrode pulverization, and the low melting points of Ca-Si alloys. The capacity fade could also be attributed to the high reactivity of CaSi, causing undesirable electrolytic side reactions.[19] Therefore, for a material to be viable as a buffer against the Si volume change it must have good electrical conductivity, medium strength, and high melting points when alloyed with Si.

Wang et al. examined both FeSi and NiSi as potential electrode materials, and proposed the following reaction mechanism for their reaction with Li:

$$xLi^+ + xe^- + MSi \rightarrow Li_xSi + M \leftrightarrow M + Si + xLi^+ + xe^-$$

where M represents the respective transition metal. These compounds yielded greater specific capacities than the disilicide compounds on first discharge, of approximately 1200 mAh $g^{-1}$ for NiSi, and better cyclability than Si powder electrodes due to the presence of the buffering material.[20]

### 3.1.2 Proposed Compounds

In contrast with previously studied calcium silicide, titanium silicides possess high electrical conductivities in addition to physical robustness as well as thermal stability, with melting points over 1500 $^oC$.[21] Anani and Huggins[22] used reported Gibbs free energy values and known binary phase diagrams to generate model ternary phase diagrams for cases in which one compound does not react with Li, and where both compounds react with Li. As Ti does not react with Li the phase diagram for this system is relatively straightforward, and lithiation from a starting composition of TiSi will yield TiSi-$Ti_5Si_3$-$Li_7Si_3$ phases in equilibrium. A desirable negative electrode material should have a high Li storage capacity and low electrode potential, to give a higher cell voltage; this system will store 1.55 Li atoms per Si atom, with an electrode potential of 0.182 V vs. Li. This potential is close to that of metallic Li, however it is not so close as to cause excessive reactivity as with $Mg_2Si$ or CaSi.

Both $TiSi_2$ and TiSi are line-phase compounds on the Ti-Si phase diagram (**Figure 3.1**), with good thermal stability. Based upon previously successful syntheses of the titanium silicides, nano-scaled $TiSi_2$ and TiSi, and their relatively high ratio between active and inactive elements, these compounds were identified as synthetic target

compounds. These compounds should contain sufficient Ti to contact and buffer the Si during lithiation, without incorporating an excess of inactive weight.

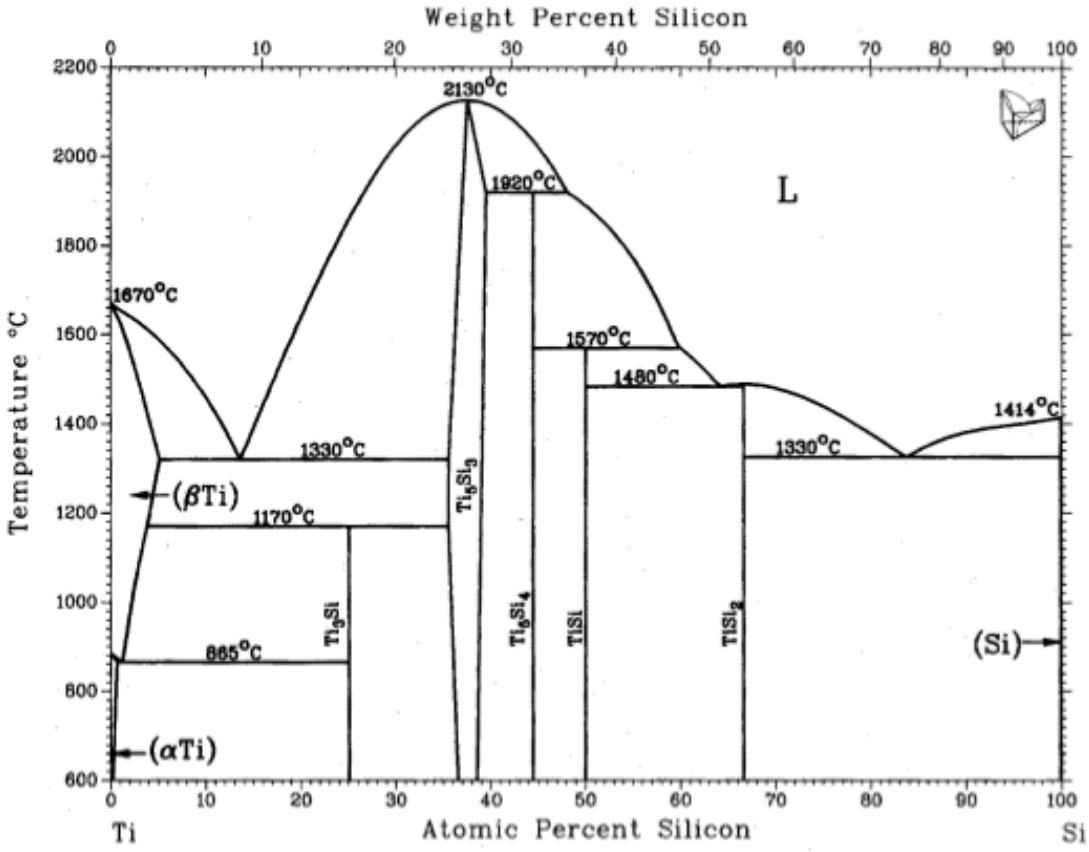


**Figure 3.1 Phase diagram of the binary Ti-Si system.[23]**

### 3.2 Experimental

#### 3.2.1 Preparation of TiSi and $TiSi_2$ Powders

Several synthetic methods have been reported for compounds within the Ti-Si system, such as chemical vapour deposition (CVD)[24,25,26], arc-casting[27,28] and inert-atmosphere annealing[28,29,30]. The attempted syntheses of line-phase compounds TiSi and $TiSi_2$ were adapted from the methods reported by Svechnikov et al. and Hansen et al.

Stoichiometric amounts of Ti (325 mesh, Aldrich, 99.7%) and Si (pieces, Aldrich, 99%) were ground in a planetary ball mill under Ar atmosphere at 200 rpm for 20 hr, with a 1:5 weight ratio between the loaded sample and stainless steel milling balls to achieve homogenous particle size and intimate mixing of the compounds. Owing to variation in reported synthetic conditions, the resultant powder was then heated in a tube furnace with changeable conditions: one of three different ambient gas mixtures – Ar, 4% $H_2$/bulk Ar, and 7% $H_2$/bulk $N_2$, and one of two annealing temperatures – 650 ºC, referred to hereafter as "low temperature" or 900 ºC, referred to as "high temperature" hereafter, were selected. Samples were cooled from their respective annealing temperature at a rate of 15 ºC/hr, with one exception rapidly quenched *via* cooling water.

### 3.2.2 Materials Characterization

Morphology and elemental analysis of the precursor and final materials were characterized by scanning electron microscopy (SEM) and energy dispersive X-ray spectroscopy (EDX), performed on a LEO 1530 field-emission SEM instrument. Powder XRD patterns were collected using a Bruker D8-Advance powder diffractometer equipped with a Vantec-1 detector, using Cu-K$\alpha_1$ radiation ($\lambda$ = 1.5406 Å). To minimize potential oxide layer formation, SEM samples were prepared in an argon glovebox and transferred in air-tight sample holders; the powder XRD samples were loaded under argon into a hermetically sealed holder equipped with a zero background silicon plate.

### 3.3 Results and discussion

#### 3.3.1 Milled Samples

Owing to the high propensity of both starting materials to form oxides, diffraction patterns of the ground samples were examined prior to annealing to check for oxidation. As seen in **Figure 3.2**, no appreciable oxidation occurred during sample milling.

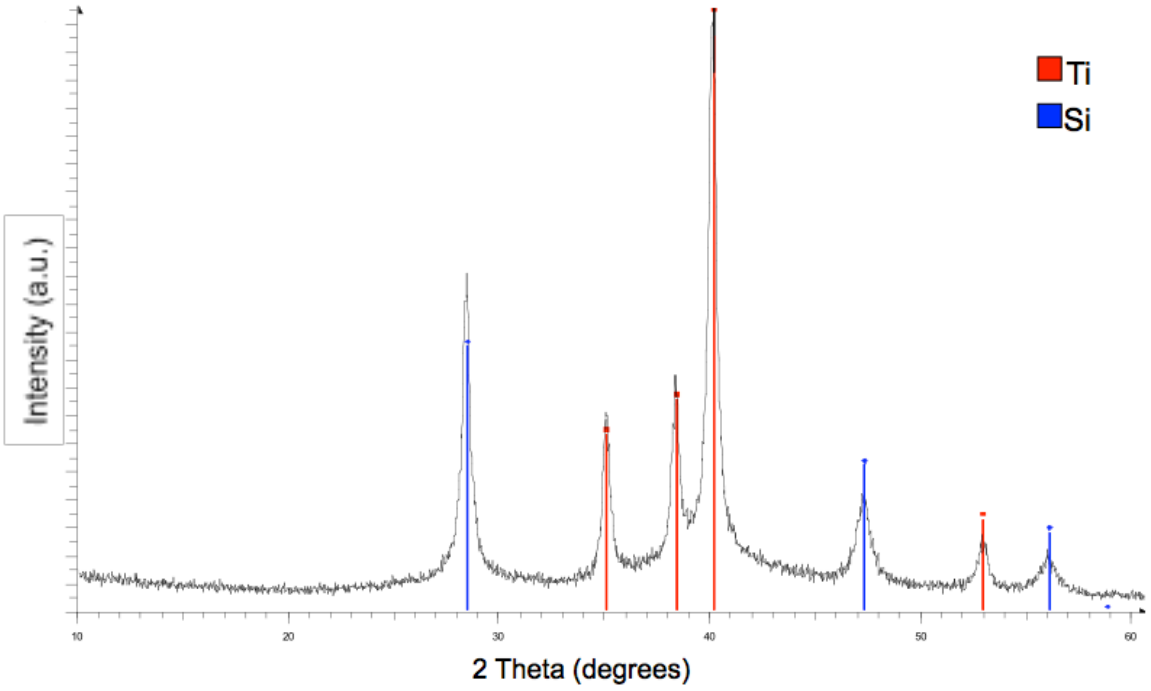


**Figure 3.2. XRD pattern of a stoichiometric mixture of Ti and Si powders following milling. Peaks corresponding to Ti powder are indicated in red, and peaks corresponding to Si are in blue.**

To ensure a consistent particle size of Si and homogenous mixture between the Ti and Si particles, the milled material was examined by SEM prior to annealing. As can be seen in **Figure 3.3**, grinding at 200 rpm for 20 hr yielded such a mixture. Additionally,

no chemical reaction between the Ti and Si powders was observed at this speed or duration.

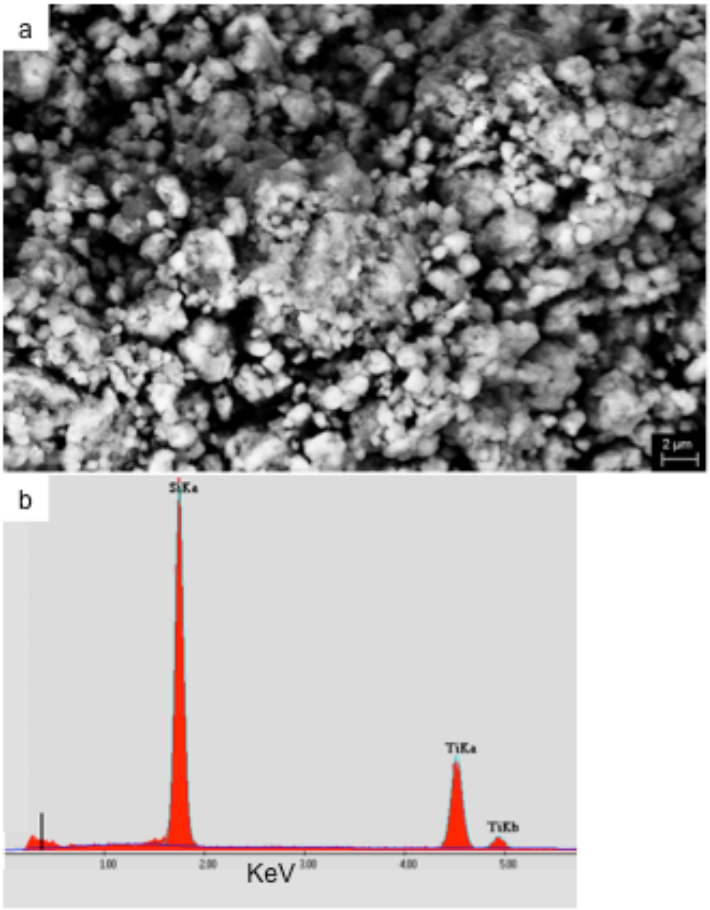


**Figure 3.3. (a) Scanning electron microscope (SEM) image of milled Ti/Si reaction mixture (scale bar = 2 µm); (b) Energy dispersive X-ray spectroscopy (EDX) image of the sample, indicating low oxygen content.**

### 3.3.2 Samples Annealed under Ar gas

Samples annealed under an atmosphere of Ar gas had a 50/50 atomic weight ratio, and were expected to yield a composition close to TiSi. However, both the high and low temperature annealed samples were composed of a mixture of $TiSi_2$ and $TiO_2$, as seen in

**Figure 3.4**. No layering of these 2 compounds was observed, as the sample appeared as a homogenous powder.

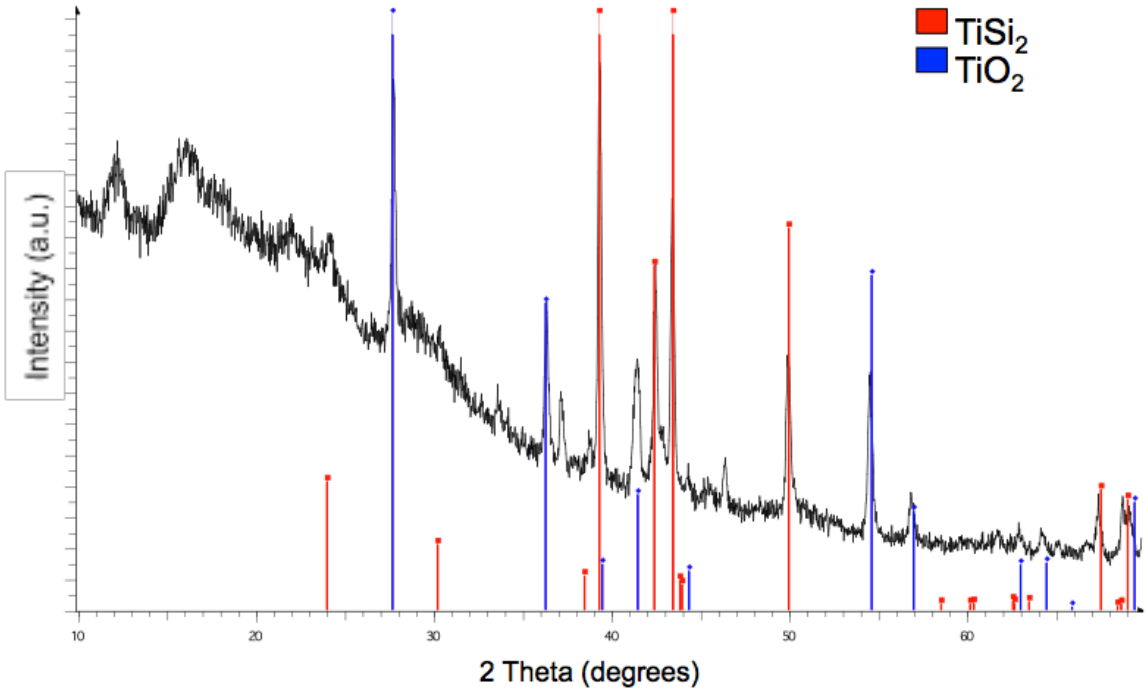


**Figure 3.4 XRD pattern obtained following high temperature annealing under Ar atmosphere of a 50/50 weight ratio Ti-Si mixture. Peaks corresponding to $TiSi_2$ are indicated in red, and peaks corresponding to rutile $TiO_2$ in blue. Unlabelled peaks below 20º have not been identified, but are believed to arise from silicon-oxide and amorphous silicon.**

Further inspection by SEM showed a thorough mixing of the compounds (**Figure 3.5**) which could not be separated by chemical etching with either HF or $HCl/H_2SO_4$. No significant oxides were found in the milled samples prior to annealing, and transfer of the milled samples to the furnace tube was done in an Ar-filled glovebox, therefore oxygen impurities were attributed to the annealing atmosphere.

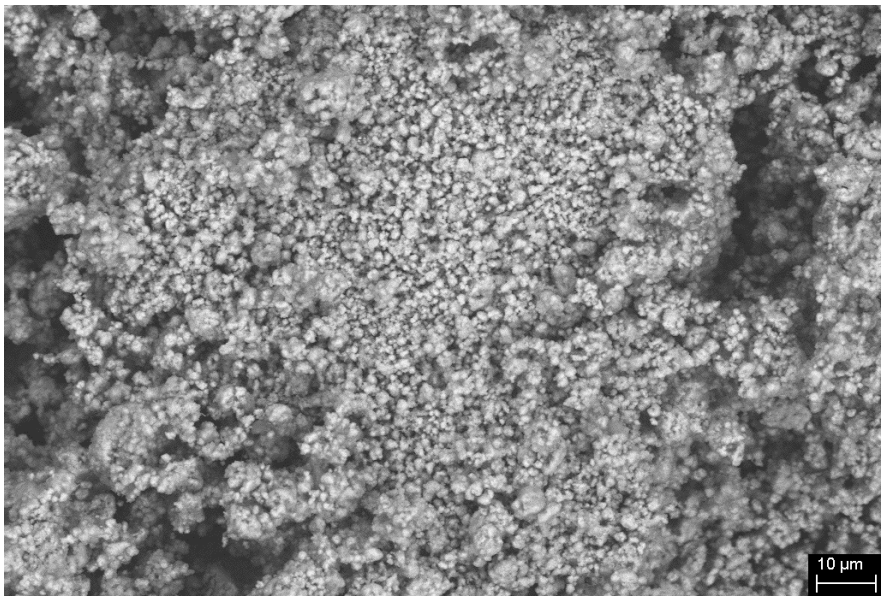


**Figure 3.5. SEM image of high temperature annealed 50/50 Ti/Si reaction mixture with Ar atmosphere (scale bar = 10 µm).**

### 3.3.3 Samples Annealed under 4% $H_2$/bulk Ar gas

Due to the oxide formation ascribed to annealing under an Ar atmosphere, the annealing ambient gas was changed to 4% $H_2$ in Ar. Through the introduction of a reducing atmosphere, it was believed that oxide growth would be suppressed. However, as shown in the diffraction patterns obtained following both low (**Figure 3.6**) and high temperature (**Figure 3.7**) annealing, $TiO_2$ was formed in both samples. This oxide growth is attributed to the extreme reactivity of Ti; difficulty in loading the samples in the furnace tube caused brief air exposure from which an oxide layer could have formed on exposed Ti particles. Titanium silicides would then have formed below this region during annealing (**Figure 3.8**).

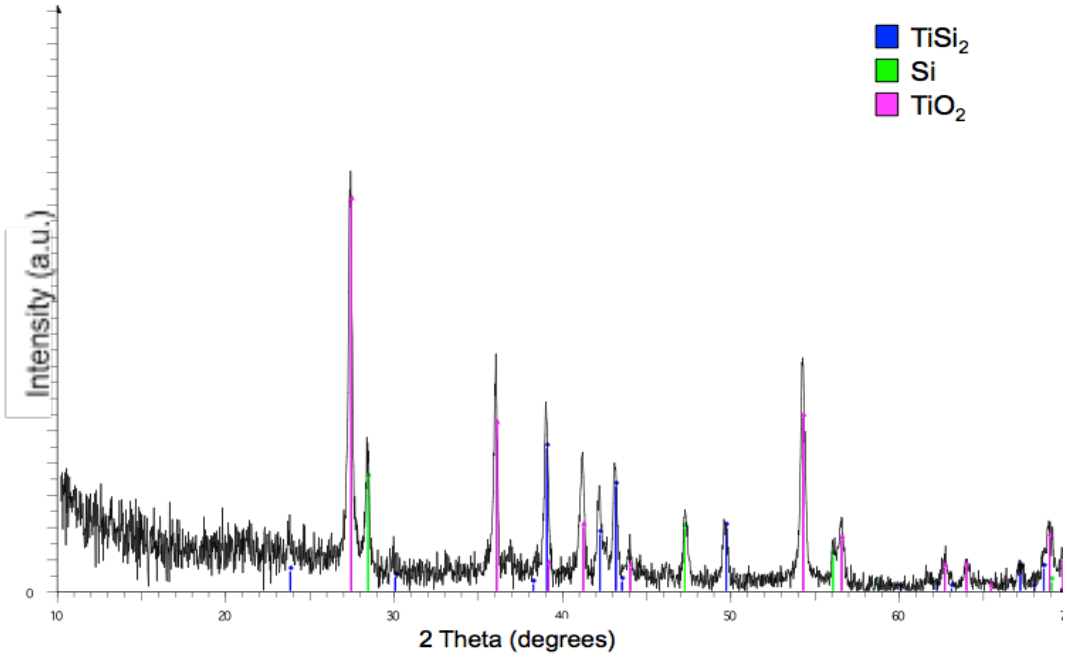


**Figure 3.6 XRD pattern obtained following low temperature annealing under 4% $H_2$ in Ar atmosphere. Peaks corresponding to $TiSi_2$ are indicated in blue, peaks corresponding to rutile $TiO_2$ are in purple, and peaks attributed to Si are in green.**

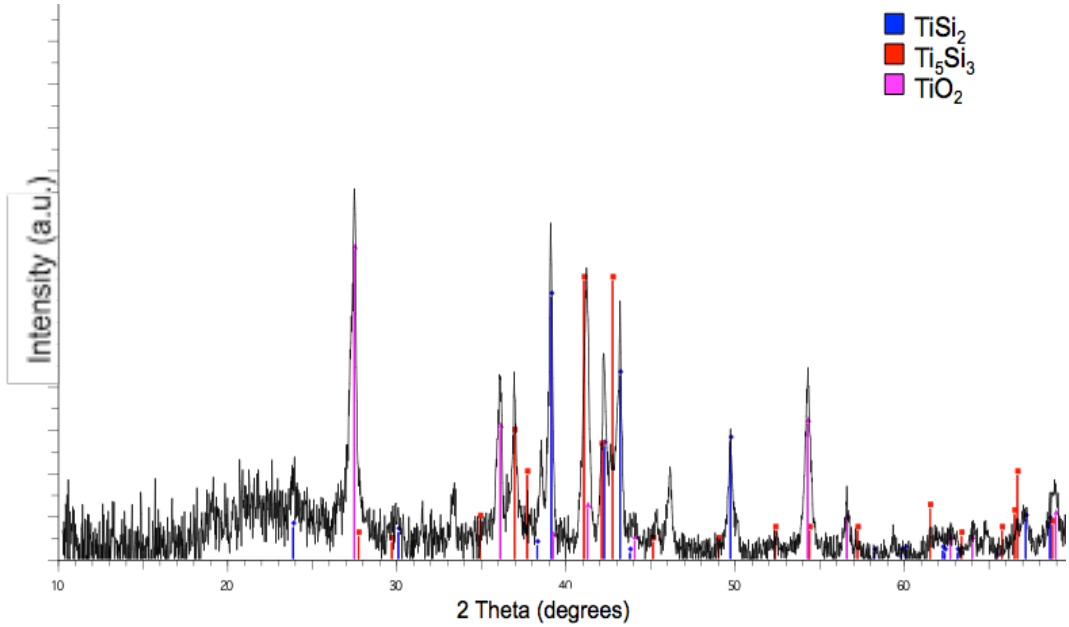


**Figure 3.7. XRD pattern obtained following high temperature annealing under 4% $H_2$ in Ar atmosphere. Peaks corresponding to $TiSi_2$ are indicated in blue, peaks attributed to rutile $TiO_2$ are in purple, and peaks corresponding to $Ti_5Si_3$ are in red.**

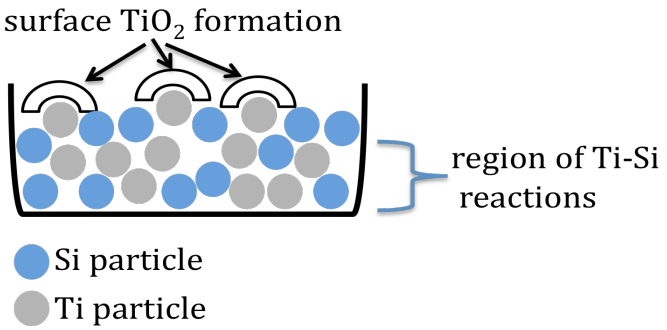


**Figure 3.8. Schematic of $TiO_2$ and Ti-Si formation for samples annealed under 4% $H_2$ in Ar.**

The products obtained from high temperature annealing yielded a mixture of $TiSi_2$ and $Ti_5Si_3$ with $TiO_2$ (**Figure 3.7**), similar to the system predicted by Anani and Huggins[22] for the lithiation of Ti-Si compounds. The product mixture was wet with N-methyl-2-pyrrolidone to make a slurry and drop cast to form a binder-free electrode. The sample was galvanostatically cycled against Li metal using a 1 M $LiPF_6$ in 1:1 (v/v) EC/DMC solution as electrolyte, between 3 V and 5 mV at a rate of C/20 as shown in **Figure 3.9**. A first discharge capacity of 715 mAh $g^{-1}$ was obtained, however rapid capacity fade can be observed upon subsequent cycles. This capacity fade is attributed to increased SEI formation, brought about by structural degradation of the electrode while cycling, as no binder was included in the electrode formulation. Due to inclusion of the electrically insulating $TiO_2$, any loss of electronic contact of active material would be amplified and further contribute to capacity fade.

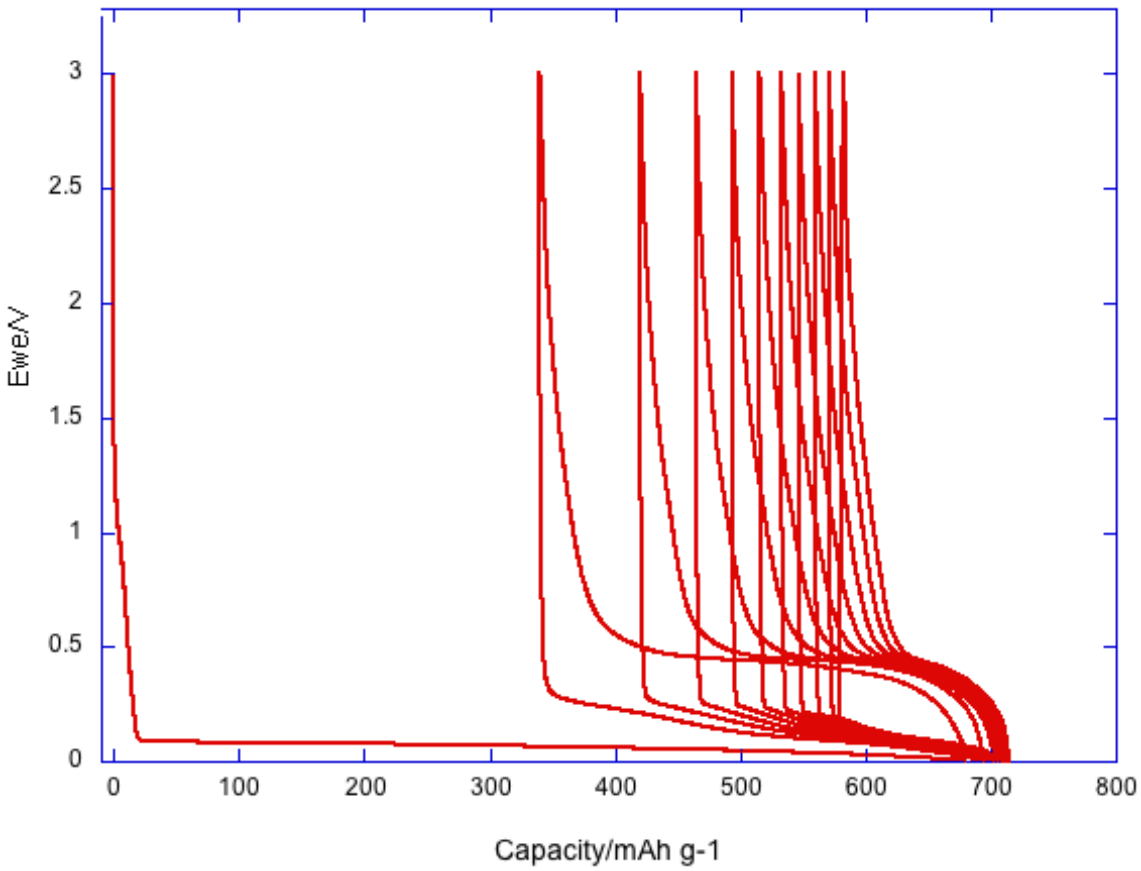


**Figure 3.9 Electrochemistry of the products produced from high temperature annealing under 4% $H_2$ in Ar gas, cycled at a rate of C/20.**

### 3.3.4 Samples Annealed under 7% $H_2$/bulk $N_2$ gas

As oxides continued to be formed with a reducing atmosphere of 4% $H_2$ in Ar, an atmosphere with a greater concentration of reducing gas was explored at the higher synthesis temperature. As the bulk of the ambient gas was $N_2$, the formation of TiN during heating was not unexpected from interactions between surface Ti particles and the atmosphere (**Figure 3.10**). In an attempt to avoid the formation of thermodynamically-favoured $TiSi_2$, the sample was rapidly quenched using cooling water. $TiSi_2$ was not observed in the diffraction pattern of the products, but another phase was identified as $Ti_3Si$, which is a line-phase compound on the Ti-Si phase diagram reported to decompose

to α-$TiSi_2$ and $Ti_5Si_3$ with nitrogen or oxygen doping.[31] While untested, it is believed that continued annealing of this sample at high temperatures followed by controlled cooling would yield a product mixture similar to that observed in **Figure 3.7**, due to atmospheric impurities during annealing.

The $Ti_3Si$ compound contains more inactive material than the target synthetic compounds; it would be unsuitable as an inactive matrix material for negative electrodes as the increased inactive matter would cause overall decreased Li storage. Both $SiO_2$ and $TiO_2$ are believed to have formed during the rapid cooling of the reaction mixture, as the system was inadvertently exposed to air.

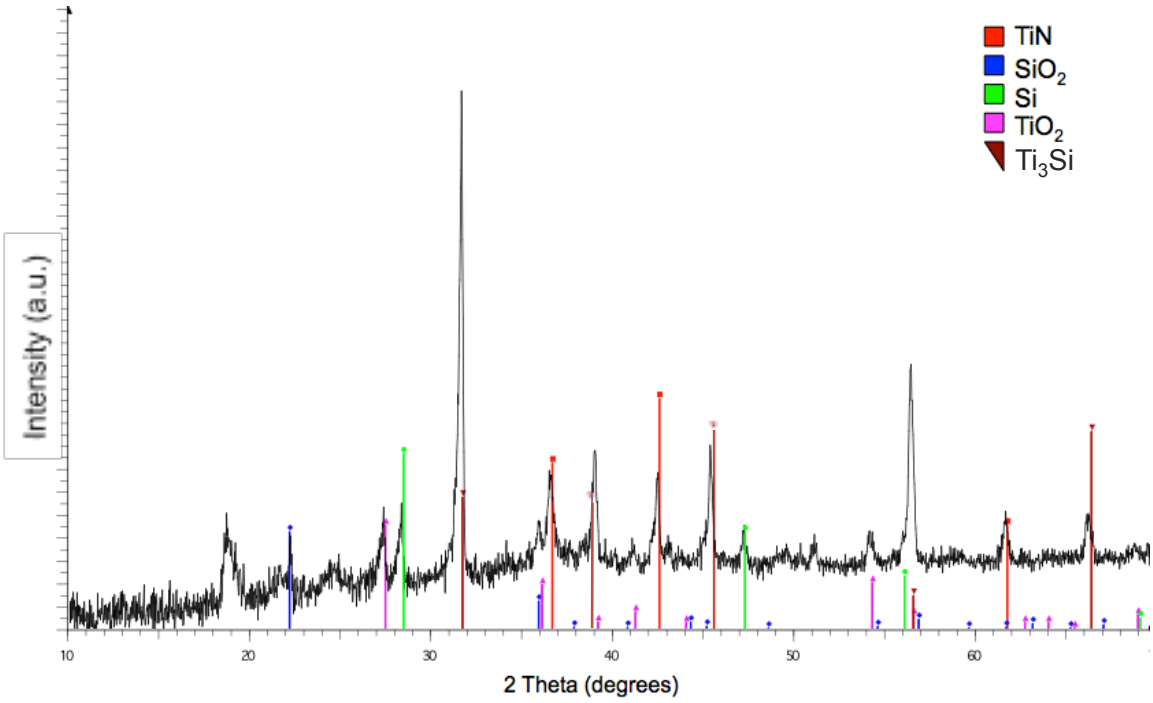


**Figure 3.10. XRD pattern obtained following annealing under 7% $H_2$ in $N_2$ atmosphere. Peaks attributed to TiN are indicated in red, $SiO_2$ in blue, crystalline Si in green, rutile $TiO_2$ in purple, and $Ti_3Si$ in brown.**

SEM images of the sample following quenching show an even dispersion of the materials in **Figure 3.11**, with a magnified image indicating the sample composition as particles of about 1 μm surrounded by thin wires. Due to slight charging observed around the particles during SEM imaging, the particles are believed to be oxides and TiN while the previously unobserved wires were attributed to preferential growth of $Ti_3Si$.

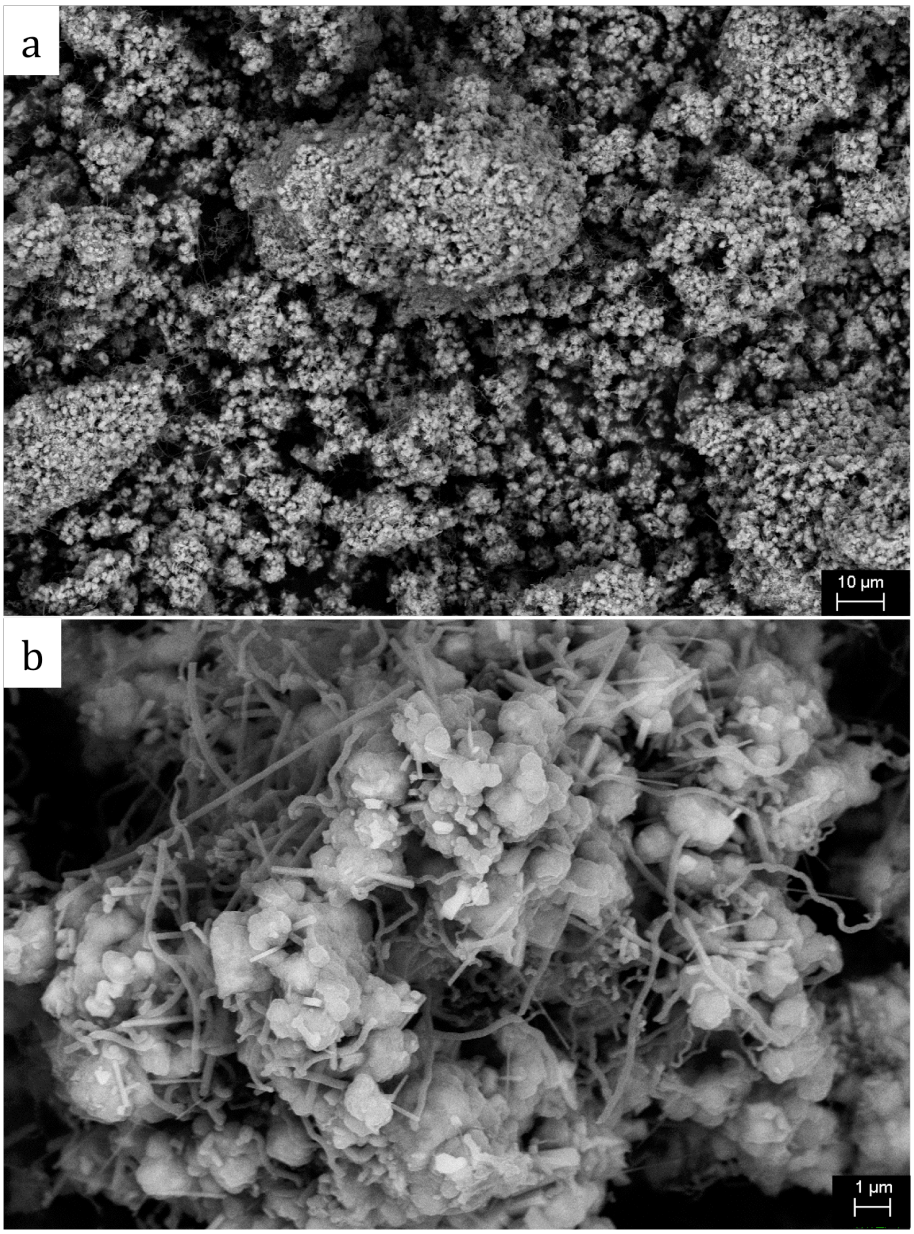


**Figure 3.11 SEM images of resultant reaction mixture obtained following annealing under 7% $H_2$ in $N_2$ atmosphere ((a) scale bar = 10 µm; (b) scale bar = 1 µm).**

### 3.3.5 Applications of $TiSi_2$ in a negative electrode

Attempts to synthesize pure TiSi and $TiSi_2$ by mechanical milling and annealing were unsuccessful in these studies. Milling of the starting materials caused no

discernable chemical reaction, and oxygen impurities introduced either in the annealing atmosphere of due to errors in sample transfer coupled with the high reactivity of Ti resulted in $TiO_2$ formation under all annealing conditions. The $TiO_2$ impurities could not be physically separated or chemically etched from the target compounds. Due to synthetic difficulties, the behaviour of these compounds as negative electrode materials was not determined. However, successful synthesis of both compounds has been previously reported, and $TiSi_2$ obtained via chemical vapour deposition (CVD) has been examined as negative electrode material.

Wang et al. have synthesized two-dimensional $TiSi_2$ structures – "nanonets" - through a chemical vapour deposition (CVD) reaction with $SiH_4$ and $TiCl_4$ precursor gases at moderate temperatures around 675ºC.[32] They have report good electrical conductivity, strength, and high surface area of the nanonets due to their morphology. The crystal structure of these nanonets is C49 $TiSi_2$, which is a metastable phase of the bulk material. It is an orthorhombic lattice system, with Si-only layers perpendicular to <010>, separated by layers of mixed Ti and Si.[33]

When the $TiSi_2$ nanonets are electrochemically cycled against Li, the Si layers in the structure act as a host for $Li^+$, observed as selective enrichment of Si on the nanonet surface, while regions with a Ti:Si ratio of 1:2 are maintained, which are used in charge transport. A specific capacity around 600 mAh $g^{-1}$ was obtained for 30 cycles with a Coulombic efficiency of 85%.[34]

Wang et al. further examined their $TiSi_2$ structures as a conductive support through galvanostatic cycling of Si-decorated nanonets. Si particles were deposited on the nanonets *via* CVD, and selectively lithiated by limiting the state of charge/discharge of

the cell. Cycling the cell between 3-0.15 V yielded a capacity of 1100 mAh $g^{-1}$ with no appreciable lithiation or degradation of the nanonet structure, however cycling between 3-0.09 V caused lithiation and eventual pulverization of the $TiSi_2$ structure.[35] The studies conducted by Wang et al.[32, 33, 34, 35] show that titanium silicides possess desirable characteristics for use in Li-ion batteries, such as good electronic conductivity and robustness as a physical support. Overall, the behaviour reported upon lithiation of the nanonet and Si/nanonet structures warrants further study of titanium silicides synthesized by CVD.

### 3.4 Conclusions

In summary, an electrochemically-active, pure Ti-Si compound was not found through the synthetic routes attempted. TiSi and $TiSi_2$ were identified as target compounds for use in Li-ion batteries containing negative electrode material supported by an inactive matrix to buffer volume changes due to lithiation/delithiation and maintain electronic connectivity. Due to the presence of oxygen introduced as an impurity in the atmosphere during annealing or a native oxide layer dispersed during grinding, $TiO_2$ impurities were consistently produced. These impurities could not be removed through etching of the samples with either HF or $HCl/H_2SO_4$ without damage to the target titanium silicide compounds. The synthesis of $TiSi_2$ nanostructures for use as a negative electrode material has been reported using CVD, a method that was not available in these studies.

One synthesized sample containing a mixture of $TiSi_2$ and $Ti_5Si_3$ with $TiO_2$ impurities was galvanostatically cycled against Li at a rate of C/20. A capacity of 715 mAh $g^{-1}$ was achieved, however rapid capacity loss over 10 cycles was observed. This

lack of robustness coupled with synthetic impurities indicates titanium silicides a poor choice as negative electrode materials for Li-ion batteries. A sample rapidly cooled from the high annealing temperature contained $Ti_3Si$, a compound unsuitable for negative electrodes due to the large amount of inactive material contained.

# Chapter 4

## Silicon-Germanium Heterostructured Nanowires

### 4.1 Motivation

As discussed in the background section, Si is an attractive negative electrode material for Li-ion batteries due to its high theoretical specific capacity. However, the method through which Li is inserted into and removed from the electrode causes a large volume change, which leads to mechanical strain and ultimately pulverization of the electrode structure over a few cycles.[36] Additional issues with Si include its intrinsically low electron conductivity and ion diffusivity, which limits the rate capability.

To mitigate these drawbacks, a one-dimensional heterogeneous structure was proposed for the electrode active material. Nanowires and nanotubes are better able to accommodate mechanical strain through radial expansion and contraction when compared with higher dimensionality or bulk Si, and can facilitate fast electron transport owing to their short Li diffusion path.[37] The incorporation of a more conductive additive such as carbon in a Si electrode is a widely used approach, as it can function as an electron transport network as well as mechanical support.[38,39] While this practice does yield improvements in capacity retention and rate capability, repeated cycling causes the eventual separation of Si and C[40]; the specific capacity of the overall electrode is also decreased due to inclusion of the conductive additive. By employing an additive that combines high conductivity with a high specific capacity, the overall energy storage of the electrode can be improved.

Germanium is a suitable negative electrode material as it can alloy with Li (**Figure 4.1**), forming several line-phase compounds analogous to the Li-Si system and yielding a theoretical capacity more than 4 times higher than graphitic carbon (1600 mAh $g^{-1}$ versus 372 mAh $g^{-1}$). It has an electrical conductivity 100 times higher than Si and a lithium diffusivity 400 times faster than Si, which makes Ge a suitable additive for a Si-based electrode[41,42].

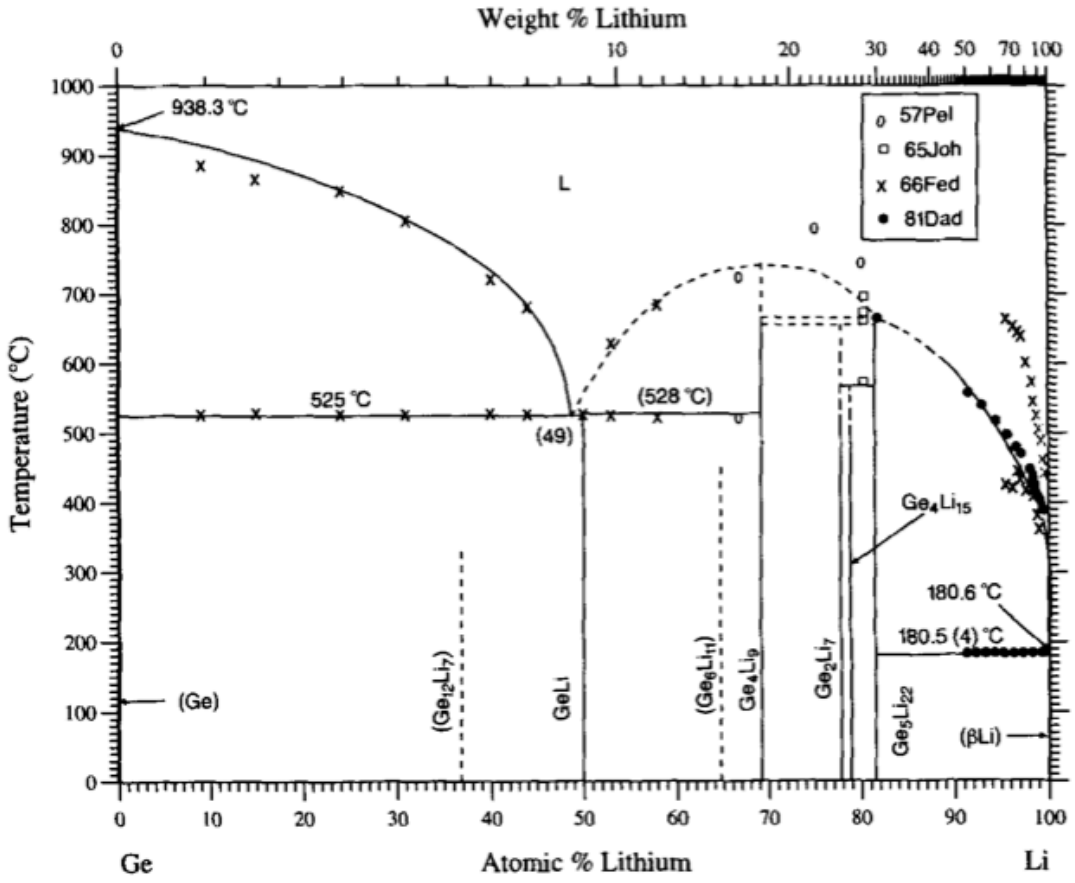


**Figure 4.1 Phase diagram of the Li-Ge system.[43]**

As Si and Ge have different reaction voltages associated with lithium, the electrochemical mechanics and kinetics of lithiation will be influenced in a heterogeneous structure. During lithiation, voltage plateaus are observed at 120 mV for crystalline Si, and 220 mV for amorphous Si.[44,45] In comparison, crystalline and amorphous Ge have

respective lithiation voltage plateaus at 250 mV and 450 mV (**Table 4.1**).[46,47] Therefore, upon lithiation a reaction with the Ge in the electrode should occur first, followed by the reaction of both Ge and Si with Li in the heterostructures. Following these alloying reactions, both amorphous $Li_xSi$ and $Li_xGe$ phases should be present in the electrode. When lithium is removed, both the core and shell of the nanowires will be an amorphous phase.

| | Crystalline | Amorphous |
|---|---|---|
| Ge | 250 mV | 450 mV |
| Si | 120 mV | 220 mV |

**Table 4.1 Associated potentials for electrochemical lithiation of Si and Ge.**

### 4.2 Experimental

#### 4.2.1 Preparation of Si-Ge and Ge-Si core-shell nanowires

The synthesis of nanostructured Si-Ge and Ge-Si core-shell nanowires was carried out by collaborators at Hanyang University in Korea. To form the structures, either Si or Ge nanowires were synthesized directly on a stainless steel substrate using the vapour-liquid-solid method. The substrate was decorated with Au colloids (20 nm diameter) as a catalyst, and placed in the quartz tube of a chemical vapour deposition (CVD) tube furnace. Either $SiH_4$ or $GeH_4$ gas was used for the synthesis of Si or Ge nanowires, respectively. To fabricate the Si-Ge core-shell nanowires, Si nanowires were first synthesized at 500 ºC and 40 Torr for 10 min. A Ge shell layer was then coated onto the Si nanowires at 360 ºC and 100 Torr for 3 min. A similar procedure was followed for the synthesis of the Ge-Si core-shell nanowires: Ge nanowires were synthesized at 300 ºC and 40 Torr for 10 min followed by a Si shell coating at 520 ºC and 20 Torr for 2 min.[48]

### 4.2.2 Materials Characterization

The nanowires were characterized as-synthesized, directly on the stainless steel substrate. Transmission electron microscopy (TEM) images were collected by collaborators at Hanyang University in Korea with a field emission transmission electron microscope (FE-TEM, JEM 2100F, JEOL) to verify the structure of the nanowires. Scanning electron microscopy (SEM) and energy dispersive X-ray spectroscopy (EDX) were performed on Ultra field-emission SEM instrument. Raman spectroscopy was collected with a LabRam HR system (HORIBA Jobin Yvon) using 633 nm laser irradiation.

### 4.2.3 Cell fabrication and electrochemical analysis

To evaluate the electrochemical performance of the Si-Ge and Ge-Si core-shell nanowires, Swagelok$^{TM}$-type half cells were fabricated with electrodes of the appropriate material described above. These electrodes were assembled against a Li metal electrode, separated by glass fiber (Whatman) which was wetted with an electrolyte solution of 1.3 M $LiPF_6$ in EC:DEC (3:7 vol %). The mass of the active material on each electrode was determined using a microbalance (Sartorius SE2, resolution 1 μg, Sartorius) to weigh the substrate before and after nanowire growth, carried out by collaborators in Korea.

Basic galvanostatic cycling of both core-shell nanowires was completed by collaborators in Korea prior to sample shipment to Canada. Si-Ge and Ge-Si nanowires were assembled in 2032 type coin cells against Li metal, with an electrolyte solution of 1.3 M LiPF6 in EC:DEC (3:7 vol %). The cells were tested between 2.0 and 0.01 V, at a rate of C/5 (TOSCAT 3000, Toyo Systems, Japan).

The electrode materials were galvanostatically cycled at a rate of C/100 between 2.5 and 0.01 V, with electrochemical impedance spectra obtained at open-circuit voltage and during lithiation at fixed cell potentials of 0.60, 0.50, 0.45, 0.40, 0.25, 0.22, 0.20, 0.12 and 0.01 V. The impedance measurements were recorded over a frequency range of 250 kHz to 10 mHz. Samples examined by potentiostatic methods were discharged to 0.01 V, with a voltage step of 10 mV. Galvanostatic Intermittent Titration Technique (GITT) samples were evaluated between 2.5 and 0.01 V, at a rate equivalent to C/50 for 15 minutes, followed by a relaxation period of 15 minutes. All electrochemical measurements were conducted on a Bio-Logic VMP3 instrument, and all cells were assembled in an argon-filled glovebox to prevent oxidation from air and moisture.

## 4.3 Results and discussion

### 4.3.1 Transmission electron microscopy, scanning electron microscopy and energy-dispersive X-ray spectroscopy

The core-shell structure of the nanowires was easily observed by collaborators in Korea immediately following synthesis using low magnification TEM (**Figure 4.2a and c**). The nanowires were measured to have a 30-40 nm core diameter, coated with a 30-40 nm shell. High resolution TEM (**Figure 4.2b and d**) showed the core of the nanowires was crystalline, while the shell consisted of amorphous material. Morphology changes due to discharge at a rate of C/5 to 0.25 V were monitored by TEM, seen in **Figure 4.3**. The Si-Ge nanowire showed slight cracking to the Si core, indicated by white arrows, while the Ge-Si sample was severely distorted due to lithiation and subsequent expansion of the crystalline Ge core.

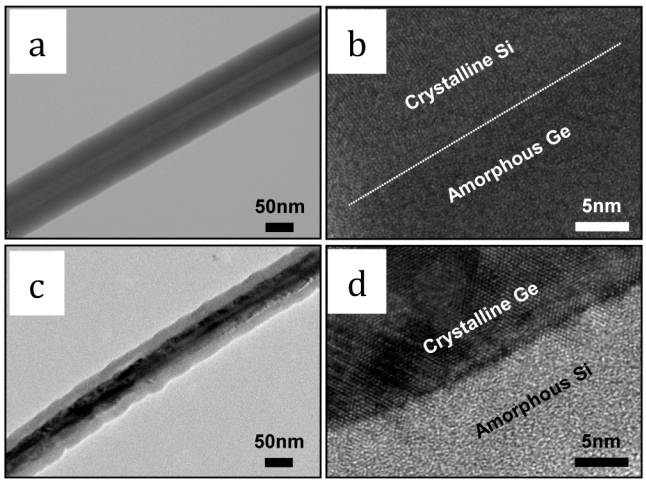


**Figure 4.2 TEM images of both Si-Ge (top) and Ge-Si (bottom) core-shell nanowires: (a) and (c) low magnification images; (b) and (d) high resolution images.**

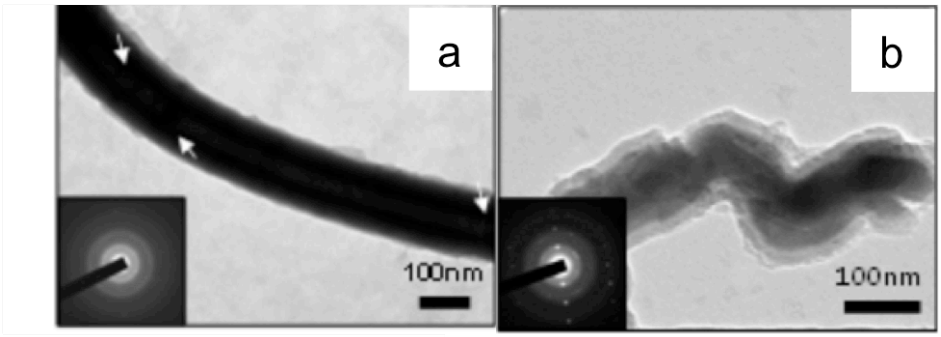


**Figure 4.3 TEM images for (a) Si-Ge and (b) Ge-Si core-shell nanowires cycled to 0.25 V. White arrows indicate the cracks due to cycling.**

Both the Si-Ge and Ge-Si nanowires possessed random growth orientation, as observed in **Figure 4.4a and b**. The composition of the nanowires and their core-shell structure was verified by a cross-sectional EDX line scan (**Figure 4.4c**). As the sample examined consisted of a Si core surrounded by a Ge shell, no significant Si signal is observed while a large signal is observed for Ge. The EDX measurements also

confirmed the absence of impurities in the samples, as the Fe signals observed on either side of the nanowire measured were due to the sample holder.

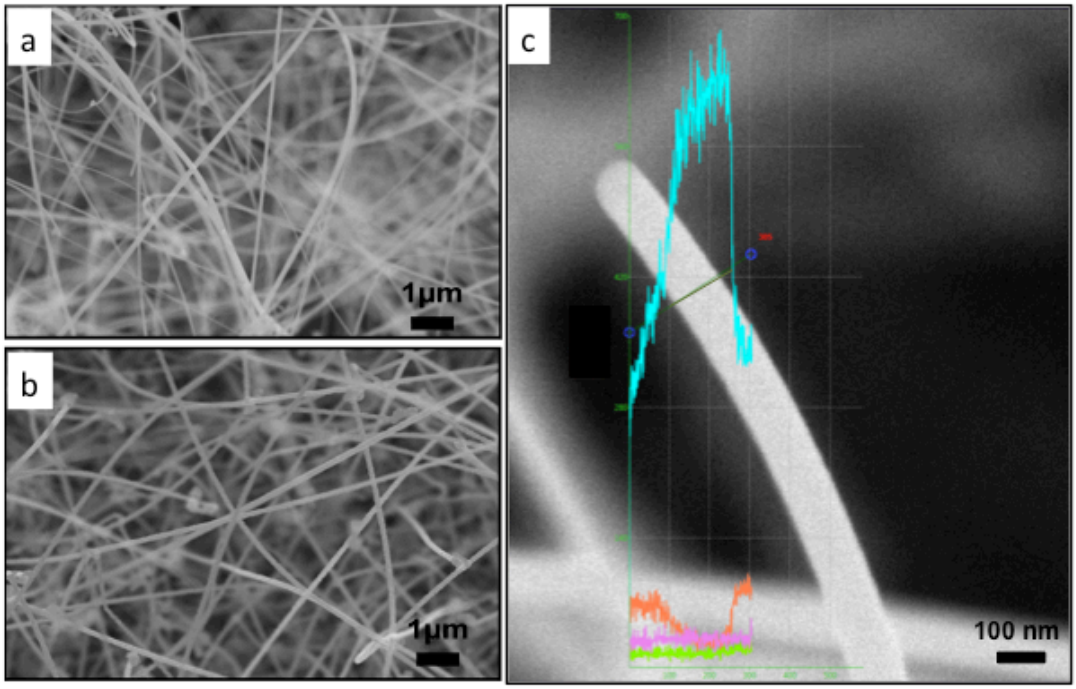


**Figure 4.4 SEM images of (a) Si-Ge and (b) Ge-Si core-shell nanowires; (c) Cross-sectional EDX elemental mapping of a Si-Ge nanowire; the line examined through the nanowire is shown in dark green. Of the elements observed, Ge is shown in light blue, Si in pink, Fe in red, and O in light green.**

### 4.3.2 Raman spectroscopy

The composition of the heterogeneous nanowires was analyzed by Raman spectroscopy, and the obtained spectra are shown in **Figure 4.5**. The Si-Ge core-shell nanowires displayed a characteristic peak around 515 $cm^{-1}$, due to the presence of crystalline Si.[49] In the spectrum of the Ge-Si core-shell nanowires, the broader peak observed at 460 $cm^{-1}$ is attributed to the amorphous Si layer on the nanowires, while the slight shoulder of the peak at 305 $cm^{-1}$ is related to the vibrations in crystalline Ge.[42]

These observations confirm the results of TEM studies, that the nanowires consist of a crystalline core coated with an amorphous shell. The absence of a signal at 490 or 600 $cm^{-1}$ due to $SiO_2$[42] or 167 $cm^{-1}$ due to $GeO_2$[49] suggests that the nanowires did not undergo oxidation prior to battery fabrication.

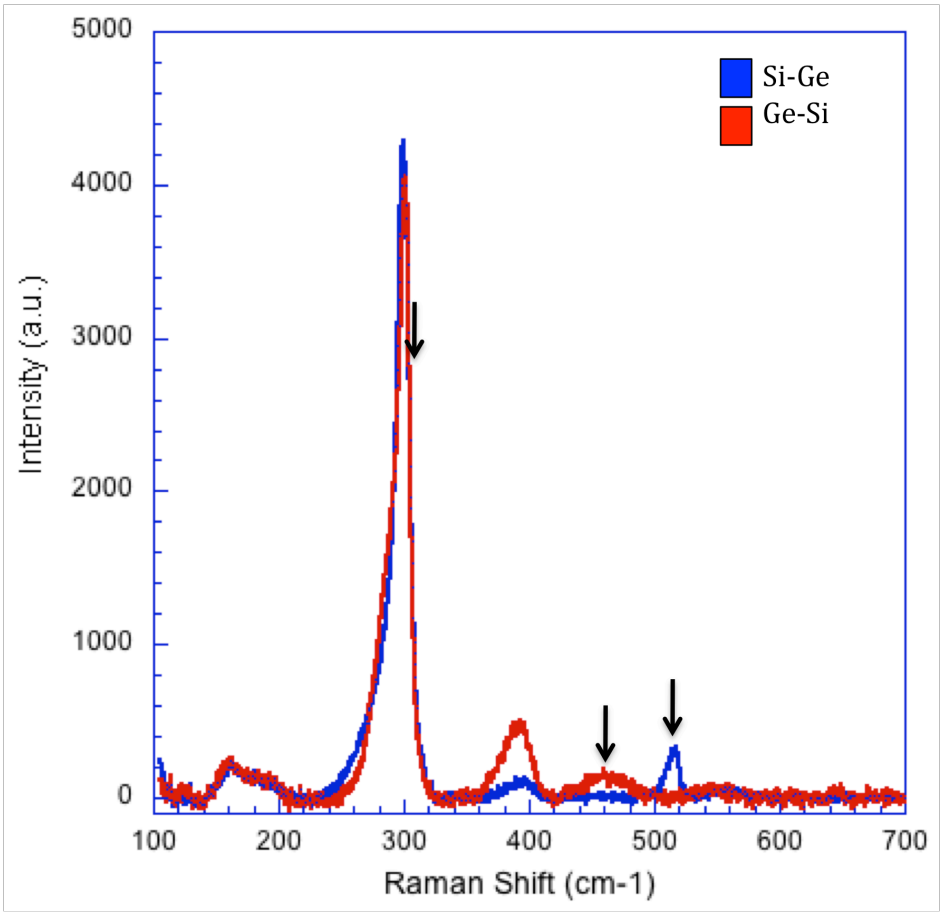


**Figure 4.5 Raman spectra of Si-Ge (blue) and Ge-Si(red) core-shell nanowires. Peaks used to identify the materials are identified with arrows.**

### 4.3.3 Galvanostatic cycling

Si-Ge and Ge-Si core-shell nanowires exhibited different, distinct voltage plateaus during charge, which arise from the different Li reactivity of both the Si and Ge (**Figure 4.6**). However, amorphization of the crystalline core of each respective electrode during the first cycle prompted identical charge-discharge curves for all subsequent cycles. In

the first cycle, the Si-Ge nanowires displayed a slightly sloped region around 0.5 V due to reaction between Li and amorphous Ge, and a short plateau at 0.19 V from lithiation of crystalling Si. Comparatively, the Ge-Si nanowires displayed a plateau at 0.25 V, attributed to reactions between Li and crystalline Ge at 0.25 V and Li and amorphous Si at 0.22 V. The Si-Ge nanowires achieved a first discharge capacity of 1346 mAh $g^{-1}$ while the complementary Ge-Si capacity was 1276 mAh $g^{-1}$.

The cycle stability of both nanowire compositions were monitored for 50 cycles (**Figure 4.6b**). After 50 cycles, the Si-Ge nanowires had a capacity retention of 72.4 % and the Ge-Si retained 62.4 %. Both core-shell nanowires displayed greater cyclabilty than previously reported Si nanowires synthesized directly on the current collector.[50] From this, it is believed that the heterogeneous system provides more favorable mechanics than a homogeneous system.

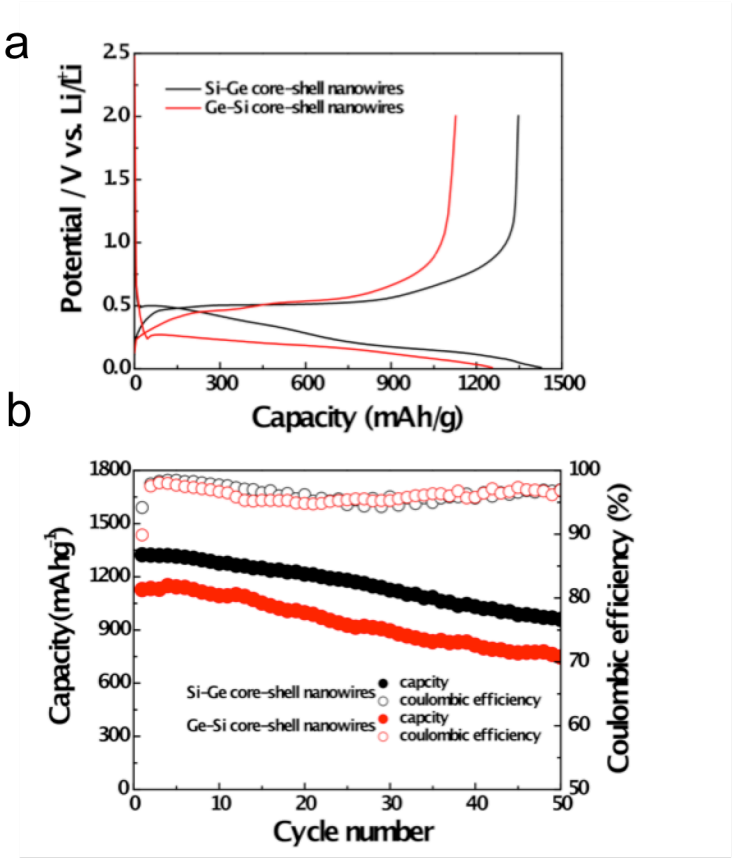


**Figure 4.6 (a) First discharge and charge capacity profiles for Si-Ge and Ge-Si nanowires, and (b) capacity retention over 50 cycles.**

### 4.3.4 Potentiostatic intermittent titration technique

While undergoing potentiostatic intermittent titration technique (PITT), the voltage of a cell is controlled to step incrementally, and the current is allowed to flow in response. Potentiostatic discharge of both the Si-Ge and Ge-Si nanowires was conducted to 0.01 V, with a voltage step of 10 mV and a time limit of 15 hr/step. A plot of integrated current versus voltage will show the quantity of charge required during lithiation, with large peaks observed at voltages that correspond to specific redox reactions or lithium insertion. During discharge, two large peaks were observed at 0.48 and 0.16 V in the current-voltage curve of the Si-Ge core-shell nanowires (**Figure 4.7**).

These peaks correspond to plateau-like regions in the discharge profile of the nanowires (**Figure 4.6a**), due to lithiation of the amorphous Ge shell and crystalline Si core of the nanowires. In the curve of the Ge-Si core-shell nanowires, peaks are observed at 0.26 and 0.18 V. These peaks align with the slightly sloping region of the discharge curve, where lithiation of the crystalline Ge core and amorphous Si shell occur, respectively.

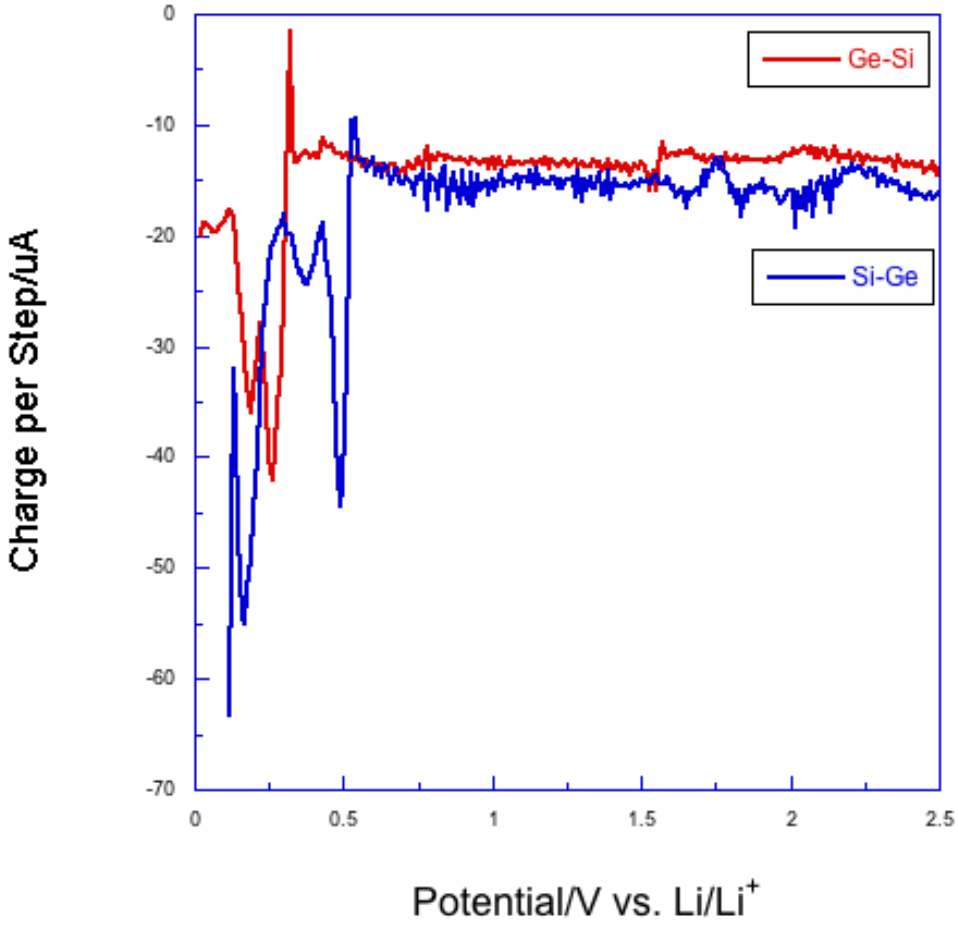


**Figure 4.7 Charge required during lithiation of Si-Ge (blue) and Ge-Si (red) nanowires. Note: due to a power outage, the Si-Ge cell was halted before 0.01 V.**

### 4.3.5 Galvanostatic intermittent titration technique

Galvanostatic intermittent titration technique (GITT) is a popular tool used to study the kinetics of a reaction, and for the calculation of diffusion coefficients. In this technique, a small current pulse is applied to the system, followed by a period of open circuit relaxation. Both the Si-Ge and Ge-Si nanowires were evaluated between 2.5 and 0.01 V, with a current equivalent to C/50 for 15 minutes followed by a relaxation of 15 minutes.

The goal of these experiments was to study and contrast the lithium alloying of Si-Ge and Ge-Si core-shell nanowires. As GITT allows for the distinction and separation of phase transitions at various Li-intercalation stages, it was employed to describe the lithium diffusion through the core-shell structure and alloying with Si and Ge.

In the calculation of the lithium ion diffusion coefficients $D_{Li^+}$, the following equation was employed:[17]

$$\tilde{D}_{Li} = \frac{4}{\pi}\left(I_0 \frac{V_m}{FS}\right)^2 \left(\frac{dE}{d\delta} / \frac{dE}{dt^{1/2}}\right)^2$$

with $I_0$ representing the polarization current, $V_m$ the molar volume of the sample, and S the surface area of a nanowire estimated using an average length of 20 μm and diameter of 105 nm. The value of $dE/d\delta$ is the slope of the coulometric titration curve found by plotting the steady-state voltages against the composition, and the short time approximation $dE/dt^{1/2}$ is only valid for times $t << L\ D$, where $L$ is the diffusion path length (diameter) of the sample.

The diffusion coefficients of lithium ions ( $D_{Li^+}$ ) in the Si-Ge and Ge-Si nanowires obtained were within the range of $10^{-16}$ to $10^{-13}$ $cm^2s^{-1}$ previously reported for group 14 compounds[51,52,53]. A slightly lower Li diffusion constant for the nanowires may be attributed to the absence of any conductive additive or binder in the electrode, as both Si and Ge are capable of alloying with and storing Li. Thus, the dense structure of the nanowires should reflect the intrinsic diffusion kinetics of Si and Ge electrodes. The obtained diffusion coefficients were then plotted against the cell potential (**Figure 4.8**), to examine the potential dependence of Li-ion diffusivity.

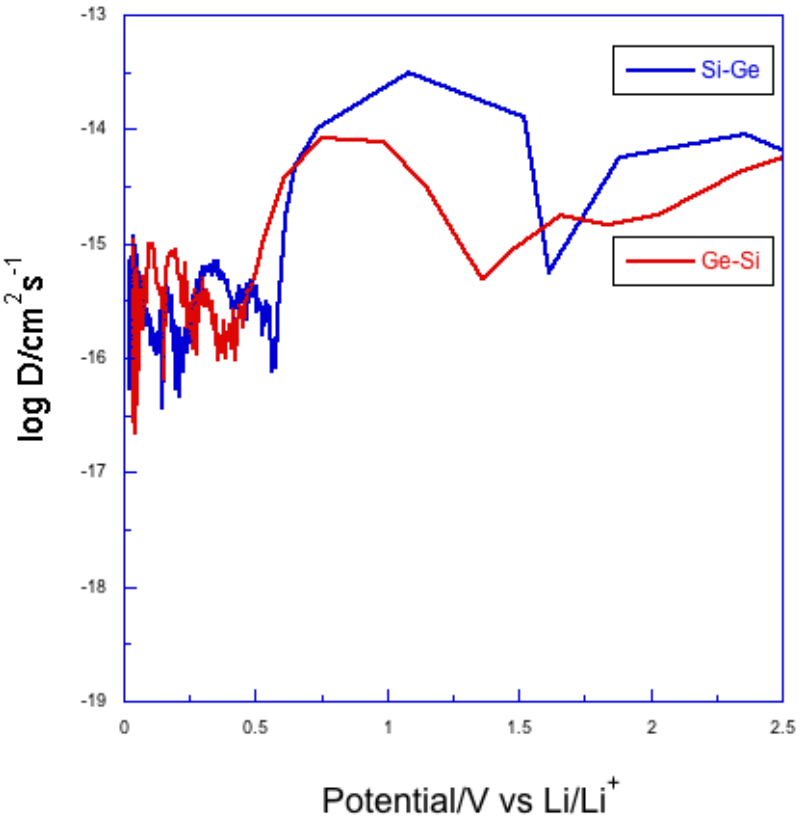


**Figure 4.8 Potential dependence of Li-ion chemical diffusion coefficients found using GITT for the Si-Ge (blue) and Ge-Si (red) core-shell nanowires.**

The initially higher value of $D_{Li^+}$ for the Si-Ge nanowires when compared with the Ge-Si core-shell nanowires is likely due to the difference in intrinsic adsorption and diffusion energies of the core materials. The higher adsorption energy of $Li^+$ on a Ge surface (4.2 eV), when compared with $Li^+$ on a Si surface (2.6 eV), causes more favourable kinetics due to a decrease in the system total energy.[54] Therefore, enhanced electrochemical kinetics are initially expected for the Si-Ge core-shell nanowires when compared to the Ge-Si core-shell nanowires.

A decrease in $D_{Li^+}$ around 1.6 and 1.3 V for the Si-Ge and Ge-Si nanowires respectively is attributed to the initial SEI formation. As the diffusion coefficient was plotted against the equilibrium potential of the cell after relaxation the onset of electrolyte breakdown to form the SEI layer appears shifted, while the total potential of the system dropped below 0.8 V during the current pulse of these steps. The fluctuation in $D_{Li^+}$ below an equilibrium potential of 0.6 V for the Ge-Si nanowires is attributed to increased $Li^+$ ion flux to both the Si shell and Ge core from cracks formed in the Si shell layer, which leads to additional SEI formation and thus an increased path length and degradation in electrochemical performance.

### 4.3.6 Galvanostatic cycling with potential limitation and electrochemical impedance spectroscopy

The discharge profile of the Si-Ge and Ge-Si nanowires on which alternating current electrochemical impedence spectroscopy (EIS) was measured can be seen in **Figure 4.9.** EIS was conducted around potentials at which significant electrochemical reactions, such as the reaction of Ge or Si with Li, and is noted on the discharge profile by black triangles. Abnormal discharge behaviour for the Si-Ge nanowire sample

(**Figure 4.9a**) above 1.75 V is attributed to temperature effects, as the controls for this sample's oven were erroneously altered.

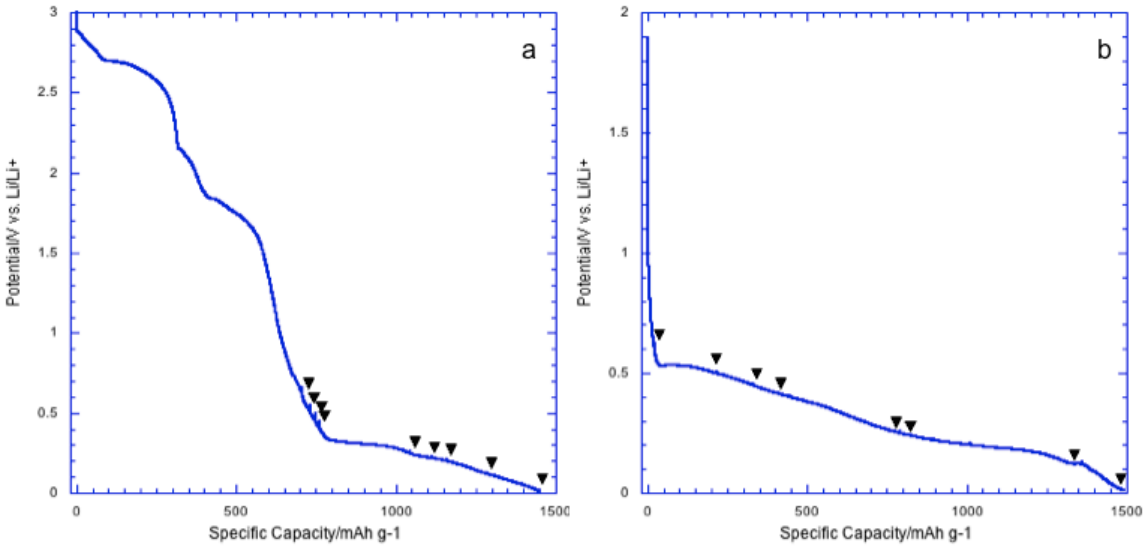


**Figure 4.9 First discharge capacity plots for (a) Si-Ge and (b) Ge-Si core-shell nanowires. Black triangles indicate position during the discharge when EIS measurements were taken.**

Using Ohm's Law and Euler's relationship, impedance can be represented as a complex number:

$$Z(\omega) = \frac{E}{I} = Z_0 \exp(j\phi) = Z_0(\cos\phi + j\sin\phi)$$

with $j = \sqrt{-1}$ and φ representing the phase difference.

As the expression for Z(ω) is composed of a real ($Z_{Re}(\omega)$) and an imaginary ($-Z_{Im}(\omega)$) part, these portions may be plotted against one another to yield a Nyquist plot. In this plot each point is the impedance at one frequency; low frequency data are shown on the right side of the plot and higher frequencies are on the left.

The resistance of an electrolyte solution is a factor in the impedance of an electrochemical cell. While a 3-electrode potentiostat compensates for the electrolyte solution resistance between the counter and reference electrode, any solution resistance between the reference and working electrodes must be considered in the model of the cell. Another component to include in the model is the charge transfer resistance, which results from the transfer of charge between the electrolyte solution and the host electrode material. The charge transfer rate is influenced by several factors, such as temperature, the concentration of reaction species, and potential. Constant phase elements within the model arise as capacitors in EIS do not behave ideally. Their behaviour is related to the inverse of the capacitance, raised to an exponent.

Diffusion can create an impedance element known as the Warburg impedance. This element depends on the frequency of the potential perturbation: at high frequencies, the Warburg impedance is small as diffusing ions have a short diffusion path. However, at low frequencies the ions have to diffuse farther, thereby increasing the Warburg impedance. On a Nyquist plot, infinite Warburg impedance would appear as a diagonal line with a slope of 0.5.

By combining these elements, an equivalent circuit of the electrochemical cell was modeled (**Figure 4.10**) and the measured impedance response of each cell was fitted (**Table 4.2**) using the Zview software.[55] In the model, $R_s$ represents all Ohmic resistance in the system, excluding the resistances of double layers and diffusion regions; this value essentially correlated to the electrolyte resistance. The Warburg impendence was represented by W, which was further divided into W-R, W-T and W-P, which are elements of the Warburg impedance that show the length of Zw with a slope of 45º, the

length of effective diffusion, and the angle of W. If W-P had a value of 1, then it would be at an angle of 90º to Z' and if W-P was 0.5 there would be infinite length Warburg. $R_{ct}$ represents Faradic charge transfer resistance for lithium insertion at the electrode/electrolyte interface or SEI, and $C_{dl}$ and CPE in circuit (a) and (b) respectively correspond to the associated electrical double layer capacitance relating to the electrode/electrolyte interface, essentially at the passive film interface. The final element in the equivalent circuit was the intercalation capacitance related to lithium diffusion in the electrode material.

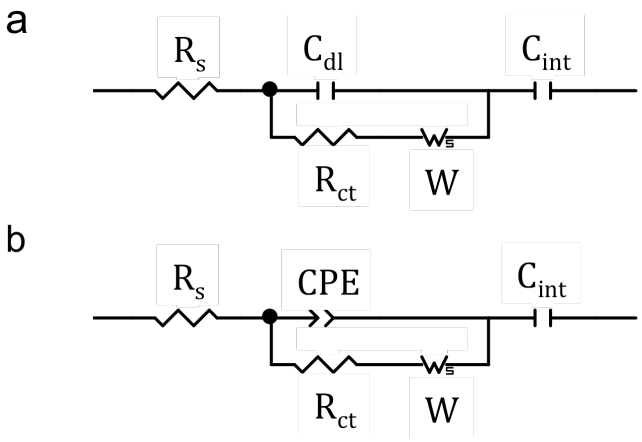


**Figure 4.10(a) and (b) Equivalent electrical circuits used to fit EIS data.**

| Potential (V vs. $Li/Li^+$) | $R_s$ ($\Omega cm^2$) | $R_{ct}$ ($\Omega cm^2$) | W-R ($\Omega cm^2 s^{1/2}$) | W-T ($\Omega cm^2 s^{1/2}$) | W-P ($\Omega cm^2 s^{1/2}$) | $C_{dl}$ or CPE ($Fcm^{-2}$;CPE-P unitless) | $C_{int}$ ($Fcm^{-2}$) |
|---|---|---|---|---|---|---|---|
| **Ge-Si** | | | | | | | |
| 0.60 | 19.01 | 208.2 | 238.1 | 1.703 | 8.221 | 4.8073E-6 | 0.01099 |
| 0.50 | 13.86 | 224.0 | 40.64 | 1.742 | 6.324 | 4.7876E-6 | 0.5543 |
| 0.45 | 10.96 | 206.5 | 89.18 | 17.64 | 0.54975 | CPE-T: 1.7666E-5<br>CPE-P: 0.84529 | 0.3674 |
| 0.40 | 13.26 | 198.0 | 88.19 | 31.13 | 0.47519 | CPE-T: 1.3832E-5<br>CPE-P: 0.87861 | 0.2102 |
| 0.25 | 11.37 | 181.1 | 54.05 | 20.81 | 0.45959 | CPE-T: 1.9402E-5<br>CPE-P: 0.84024 | 0.2999 |
| 0.22 | 11.03 | 187.2 | 40.62 | 13.3 | 0.48219 | CPE-T: 2.1096E-5<br>CPE-P: 0.82868 | 0.2989 |
| 0.20 | 11.26 | 196.7 | 38.64 | 11.36 | 0.49128 | CPE-T: 2.1501E-5<br>CPE-P: 0.82533 | 0.3125 |
| 0.12 | 11.26 | 177.1 | 83.95 | 19.05 | 0.52861 | CPE-T: 2.3381E-5<br>CPE-P: 0.81888 | 0.1559 |
| 0.01 | 11.37 | 176.2 | 41.33 | 10.36 | 0.48109 | CPE-T: 2.4346E-5<br>CPE-P: 0.81373 | 0.4160 |
| **Si-Ge** | | | | | | | |
| 0.60 | 12.76 | 310.0 | 411.7 | 0.9038 | 0.54773 | 2.9520E-6 | 0.003169 |
| 0.50 | 17.49 | 188.5 | 1964 | 32.24 | 0.40723 | 2.8806E-6 | 0.01330 |
| 0.45 | 17.01 | 172.0 | 201.0 | 32.74 | 0.39042 | 2.7121E-6 | 0.01560 |
| 0.40 | 9.684 | 254.4 | 1036 | 4.876 | 0.45346 | CPE-T: 3.7898-5<br>CPE-P: 0.69304 | 0.08100 |
| 0.25 | 11.25 | 181.7 | 393.8 | 30.38 | 0.42276 | CPE-T: 3.8804E-5<br>CPE-P: 0.73285 | 0.13383 |
| 0.22 | 10.23 | 182.7 | 224.6 | 8.140 | 0.48564 | CPE-T: 4.7324E-5<br>CPE-P: 0.7108 | 0.08876 |

| | | | | | | | |
|---|---|---|---|---|---|---|---|
| 0.20 | 10.30 | 183.0 | 187.6 | 9.673<br>10.22 | 0.42232 | CPE-T: 4.689E-5<br>CPE-P: 0.7118 | 0.08334 |
| 0.12 | 10.51 | 194.3 | 209.8 | 9.412 | 0.44586 | CPE-T: 4.7753E-5<br>CPE-P: 0.71053 | 0.08663 |
| 0.01 | 10.40 | 190.0 | 182.6 | 21.44 | 0.27149 | CPE-T: 4.4358E-5<br>CPE-P: 0.71579 | 0.06303 |

**Table 4. 2 Elements of equivalent circuits for EIS measurements of Si-Ge and Ge-Si nanowires.**

While it is preferable to use capacitance in modeling a system, samples examined by EIS corresponding to a lower cell potential required the introduction of a constant phase element due to an increased SEI layer. This was evident in the Nyquist plot of the samples (**Figure 4.11**), as the high frequency semicircle was deformed for samples measured at lower potentials. The Nyquist plots also show a decrease in resistance of the Si-Ge nanowires below 0.45 V; this phenomenon is related to the lithiation of the Ge shell at 0.45 V, increasing conductivity in the material as the Li-Ge alloy is formed. No large drop in resistance is observed for the Ge-Si nanowires. In the Ge-Si heterostructured nanowires the Ge will react with Li before the Si in the compound, however Ge is at the core of this material and therefore requires Li diffusion through the amorphous Si shell before alloying can commence.

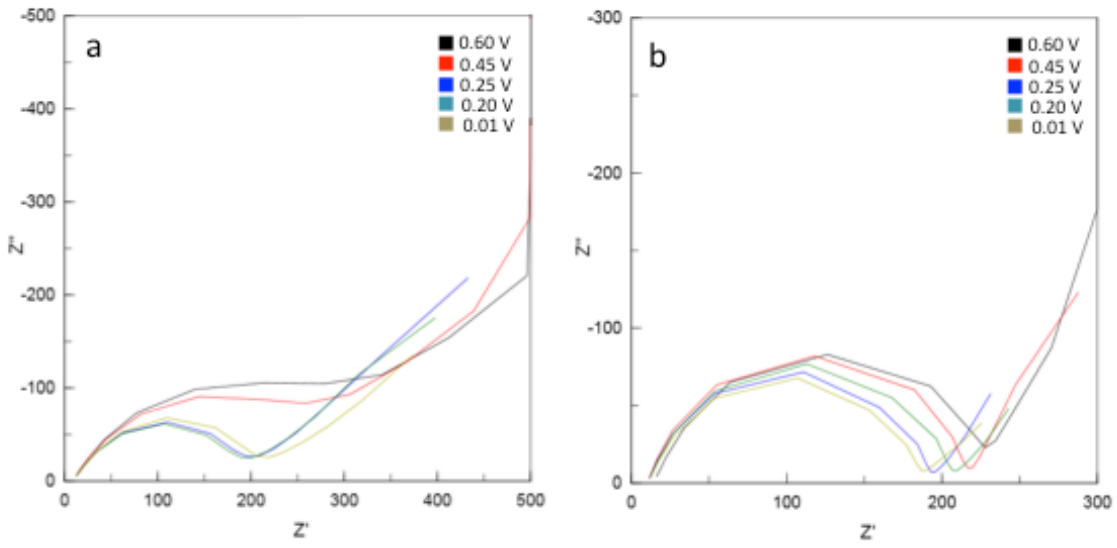


**Figure 4.11 Representative AC impedance Nyquist plots of (a) Si-Ge and (b) Ge-Si core-shell nanowires paused at various states of lithiation.**

Using the Warburg impedance, the diffusion coefficient of lithium ions into the electrode active material can be calculated:[56]

$$W_T = \frac{L^2}{D_{Li}}$$

using W-T as described above and $L$ as the diffusion path length. The diffusion coefficients calculated are plotted against the potential they were measured at in **Figure 4.12**.

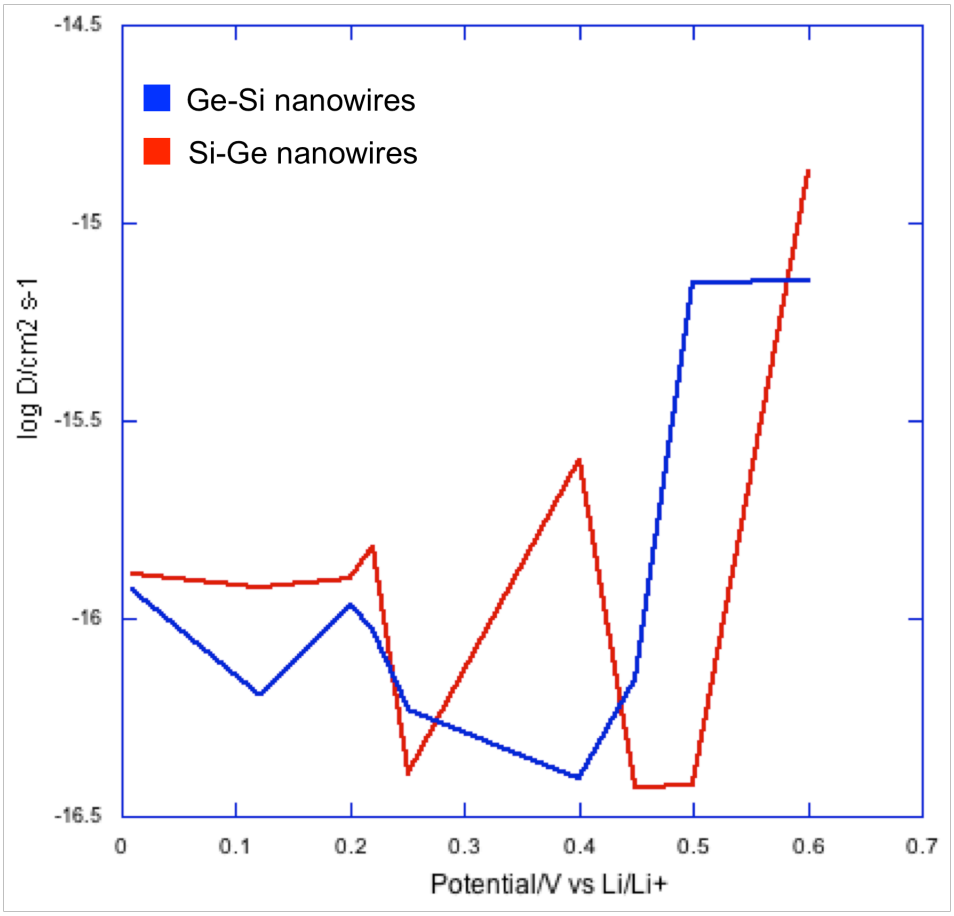


**Figure 4.12 Potential dependence of Li-ion chemical diffusion coefficients found using EIS for the Ge-Si (blue) and Si-Ge (red) core-shell nanowires.**

The lithium diffusion coefficients found via EIS are within the same accepted range of values as those found via GITT. For both the Si-Ge and Ge-Si nanowires, $D_{Li^+}$ decreases around 0.6 V to about 0.4 V due to the formation of the SEI layer; owing to the highly exposed morphology of nanowires the SEI formation is considerable. When the electrode material begins to react with Li, around 0.4 V for the Si-Ge nanowires and 0.25 V for the Ge-Si nanowires, $D_{Li^+}$ increases due to increased conductivity. This effect is more pronounced for the Si-Ge nanowires than for the Ge-Si nanowires, as the surface layer and not the core is reacting. At approximately 0.23 V $D_{Li^+}$ decreases again for the Si-Ge sample, due to an increased path length as the core of the material reacts with Li. This effect is not as pronounced for the Ge-Si sample, as Li was already required to pass through the Si shell to react with Ge.

### 4.4 Conclusions

Heterostructured Si-Ge and Ge-Si nanowires were successfully synthesized by collaborators using a vapour-liquid-solid method. The aim of the research was to accommodate the mechanical strain associated with lithiation/delithiation of Si through the morphology of the compound, without sacrificing a high specific capacity and improving the electronic contact within the material.

The electrochemistry of the nanowires was thoroughly analyzed through galvanostatic cycling, PITT, GITT and EIS. Discharge capacities achieved for the heterogeneous nanowires are greater than that of graphitic carbon or homogenous nanowires, however both the Si-Ge and Ge-Si nanowires fall short of the theoretical specific capacity of either Si or Ge. Lithium diffusion coefficients calculated from GITT

and EIS measurements were in the range of $10^{-16}$ to $10^{-13}$ $cm^2s^{-1}$, in accordance with other reported values for group 14 compounds.

## Future Perspectives

The focus of the work presented in this thesis was on Si-based materials for use as negative electrodes in Li-ion batteries. Portable electronic devices are becoming increasingly important in daily life, which requires small, lightweight energy storage devices such as the Li-ion battery; Li-ion batteries are also being employed in large-scale applications such as hybrid and pure electric vehicles. Development of Si electrodes that are low cost with a high specific capacity will help to meet energy storage needs in the near future.

In the first part of the thesis, titanium silicides were pursued as inactive matrix compounds to help buffer the volume expansion of Si on lithiation. The target compounds were not synthesized and could not be isolated through etching, however one product mixture was cycled against Li. A capacity of 715 mAh $g^{-1}$ was achieved, however rapid capacity fade occurred over the first 10 cycles. Other compounds from this class of materials, such as nanonet $TiSi_2$, have been successfully synthesized through CVD and show promise as negative electrode materials due to their unique structure. Therefore, there is potential for two-dimensional nano-scaled binary compounds as negative electrode materials and further development of $TiSi_2$ nanonets holds promise.

The second part of the thesis focused on heterostructured Si-Ge and Ge-Si core-shell nanowires, in which the Ge functions as an active matrix, since it can alloy with Li. The specific capacity of the nanowires were good at 1346 mAh $g^{-1}$ and 1276 mAh $g^{-1}$, however after 50 cycles the Si-Ge nanowires had a capacity retention of 72.4 % and the Ge-Si retained 62.4 %. The diffusion coefficient of Li was determined from GITT and

EIS and was slightly lower than other reported values; the dense structure of the nanowires could cause slower diffusion. Future research should continue to examine other Si-Ge nanostructures for increased electronic contact and increased diffusion.

There are still many issues, such as initial cycle efficiency, and poor cyclability that need to be addressed in future research. However, due to the limitations of carbon as a negative electrode material, particularly for large-scale applications, there is a great demand for new negative electrode materials to improve the performance of Li-ion batteries.

# References


[1] Whittingham, M. S. *Science*, **192**, 1126 (1976).

[2] Tarascon, J.-M., Armand, M. *Nature,* **414**, 359 (2001).

[3] Dey, A. N., *J. Electrochem. Soc*., **118**, 1547, (1971).

[4] Li, J., Dahn, J. R. *J. Electrochem. Soc.,* **154**, A156, (2007).

[5] Okamoto, H., *Journal of Phase Equilibria and Diffusion*, **30**, 118, (2009).

[6] Datta, M. K., Kumta, P. N., *J. Power Sources,* **194**, 1043 (2009).

[7] Key, B., Bhattacharyya, R., Morcrette, M., Seznéc, V., Tarascon, J.-M., Grey, C. P. *J. Am. Chem. Soc.,* **131,** 9239, (2009).

[8] Bridel, J.-S., Azaias, T., Morcrette, M., Tarascon, J.-M., Larcher, D. *Chem. Mater.,* **22**, 1229, (2010).

[9] Kasavajjula, U., Wang, C., Appleby, J. *J. Power Sources,* **163**, 1003, (2009).

[10] Ryu, J. H., Kim, J. W., Sung, Y.-E., Oh, S. M. *Electrochem. Solid State Lett.,* **7**, A306 (2004).

[11] Hatchars, T. D., Obrovac, M. N., Dahn, J. R., *J. Electrochem. Soc*., **153**, A282, (2006).

[12] Maranchi, J. P., Hepp, A. F., Kumta, P. N., *Electrochem. Solid State Lett*., **6** A198 (2003).

[13] Lee, J. K., Kung, M. C., Trahey, L., Missaghi, M. N. Kung, H. H., *Chem. Mater*., **21** 6 (2009).

[14] Magasinski, A., Dixon, P., Hertzberg, B., Kvit, A., Ayala, J., Yushin, G., *Nat. Mater*., **9** 353 (2010).

[15] W. L. Bragg, *Proc. Camb. Phil. Soc.,* **17**, 43, (1913).

[16] Davoisine, C., Dupont, L. *SEM and TEM - Unpublished lecture notes;* Université Picardie Jules Verne, (2009).

[17] Weppner, W., Huggins, R.A., *J. Electrochem. Soc*., **124** 1569 (1977).

[18] Kasavajjula, U., Wang, C., Appleby, J., *J. Power Sources,* **163**, 1003, (2009).

[19] Netz, A., Huggins, R., Weppner, W., *J. Power Sources,* **119-121**, 95, (2003).

[20] Wang, G. X., Sun, L, Bradhurst, D. H., Zhong, S., Dou, S. X., Liu, H. K., *J. Power Sources*, **88**, 278, (2000).

[21] Dabrowski, J., Müssig, H.-J. *Silicon Surfaces and Formation of Interfaces,* World Scientific Publishing, London, U.K., 330 (2000).

[22] Anani, A., Huggins, R. A., *J. Power Sources*, **38,** 351, (1992).

[23] Massalski, B., Subramanian, P.R., Okamoto, H., *Binary Alloy Phase Diagrams, 2nd ed*., Vol. 1 - 3, ASM International, Materials Park, 3367, (1990).

[24] Zhou, S., Liu, X., Lin Y., Wang, D., *Angew. Chem. Int. Ed.,* **47,** 7681, (2008).

[25] Zhou, S., Liu, X., Lin Y., Wang, D., *Chem. Mater.,* **21.** 1023, (2009).

[26] Du, J., Ren, Z., Tao, K., Hu, A., Hao, P., Huang, Y., Zhao, G.,Weng, W., Han,G., Du, P. *Crystal Growth and Design,* **8**, 3543, (2008).

[27] Hansen, M., Kessler, H. D., McPherson, D. J. *Transactions of the American Society for Metals,* **44**, 518, (1952).

[28] Svechnikov, V.N., Kocherzniskii, Y.A., Shishkin, E.A. *Doklady Akademii Nauk SSSR*., **193**, 393, (1970).

[29] Zhou, H. Li, B., Yang, Z. Zhan, N., Yan, D., Lake, R. K., Liu, J. *IEEE Trans. on Nanotech.,* **10** 499, (2011).

[30] Zhang, S.-L., Lavoie, C., Cabrel Jr., C., Harper, J.M.E., d'Heurle, F.M. Jordan-Sweet, J., *J. Appl. Phys*., **85**, 2617m (1999).

[31] Da Silva Costa, A. M., de Lima, G. F., Rodrigues, G. Nunes, C. A., Coelho, G. C., Suzuki, P. A., *Journal of Phase Equilibria and Diffusion*, **31**, 22, (2010).

[32] Zhou, S., Liu, X., Lin, Y., Wang, D., *Angew. Chem. Int. Ed.,* **47**, 7681, (2008).

[33] Zhou, S., Liu, X., Lin, Y., Wang, D., *Chem. Mater*., **21**, 1023, (2009).

[34] Zhou, S. Wang, D., *ACS Nano*, **4**, 7014, (2010).

[35] Zhou, S., Liu, X., Wand, D., *Nano Lett.*, **10**, 860 (2010).

[36] Boukamp, B. A., Lesh, G. C., Huggins, R. A., *J. Electrochem. Soc.,* **128**, 725, (1981).

[37] Cui, L. F., Ruffo, R., Chan, C. K., Peng, H. L., Cui, Y. *Nano Lett.*, ***9***, 491 (2009).

[38]Cui, L. F. Yang, Y., Hsu, C. M., Cui, Y., *Nano Lett.,* **9**, 3370, (2009).

[39] Park, C.-M., Kim, J.-H., Kim, H., Sohn, H.-J., *Chem. Soc. Rev.,* **39**, 3115, (2010).

[40] Wang, X., Yao, J., Liu, H. K., *Electrochem. Solid-State Lett.* **7**, A250, (2004).

[41] Graetz, J., Ahn, C. C., Yazami, R., Fultz, B., *J. Electrochem. Soc.,* **151,** A698, (2004).

[42] Seng, K. H., Park, M.-H., Guo, Z. P., Liu, H. K., Cho, J. *Angew. Chem. Int. Ed.,* **51**, 5657, (2012).

[43] Sangster, J., Pelton, A. D., *J. Phase Equilib.*, **13**, 289, (1997).

[44] Esmanski, A., Ozin, G. A. *Adv. Funct. Mater.,* **19**, 1999, (2009).

[45] Gao, B., Sinha, S., Fleming, L., Zhou, O., *Adv. Mater.,* **13***,* 816*, (*2001**).**

[46] Seo, M. H., Park, M., Lee, K. T., Kim, K., Kim, J., Cho, J., *Energy & Environmental Science*, **4**, 425, (2011).

[47] Cui, G. L., Gu, L., Zhi, L. J., Kaskhedikar, N., van Aken, P. A., Mullen, K., Maier, J. *Adv. Mater.*, **20**, 3079, (2008).

[48] Song, T., Cheng, H., Town, K., Park, H., Black, R.W., Lee, S., Park, W.I., Huang, Y., Rogers, J.A., Nazar, L.F., Paik. U., *Adv. Funct. Mater.,* in press, (2013).

[49] Prades, J. D., Arbiol, A., Cirera, A., Morante, J. R., Fontcuberta I Morral, A. *Appl. Phys. Lett.*. **91**, 123107, (2007).

[50] Kang, K., Lee, H. S., Han, D. W., Kim, G. S., Lee, D., Lee, G., Kang, Y. M., Jo, M. H., *Appl. Phys. Lett.,* **96**, (2010).

[51] Green, M., Fielder, E., Scrosati, B., Wachtler, M., Moreno, J.S. *Electrochem. Solid-State Lett.,* **6**, A75, (2003).

[52] Kulova, T. L., Skundin, A. M., Pleskov, Y. V., Terukov, E. I., Kon'kov, O. I. J *Electroanalytical Chemistry*, **217**, 600, (2007).

[53] Manjunatha, H.; Mahesha, K. C.; Suresha, G. S.; Venkateshab, T. V., *Electrochim. Acta,* **80***,* 269, (2012).

[54] Song, T., Cheng, H. Y., Choi, H., Lee, J. H., Han, H., Lee, D. H., Yoo, D. S., Kwon, M. S., Choi, J. M., Doo, S. G., Chang, H., Xiao, J. L., Huang, Y. G., Park, W. I., Chung, Y. C., Kim, H., Rogers, J. A., Paik, U., *ACS Nano,* **6**, 303, (2012).

[55] Zview for Windows, Scribner Associates, Inc, Virginia, (1994).

[56] Macdonald, J. R., *Annals of Biomedical Engineering*, **20**, 289, (1992).